

## Cover letter

4 October 2021

To  
Editor, Materials and Metallurgical Transactions A

From  
Dr. Anish Upadhyaya  
Professor  
Department of Materials Science and Engineering  
Indian Institute of Technology Kanpur 208016 UP  
[anishu@iitk.ac.in](mailto:anishu@iitk.ac.in)

Dear Sir,

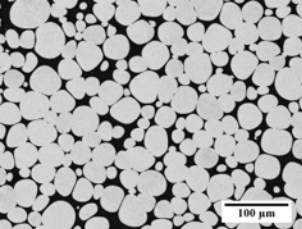
We wish to submit an original research article entitled “Texture evolution during uniaxial compression of tungsten heavy alloys” for consideration for publication as regular article in your journal. This paper is based on the doctoral research work carried out by the co-author Mr. Mirtunjay Kumar in our guidance (Drs. NP Gurao and A. Upadhyaya). On behalf of all the coauthors, I confirm that this work is original and has not been published elsewhere, nor is it currently under consideration for publication elsewhere.

This paper investigated the crystallographic texture evolution of tungsten heavy alloy in compression load. This study is significant because WHA undergoes a large deformation upon ballistic impact. So, a systematic investigation of the deformation of this heavy alloy is needed. As crystallographic texture evolution during processing plays a vital role in the mechanical behaviour of the alloy, we compressed the W-Ni-Fe heavy alloy where tungsten content varied from 80 to 98 and captured the texture with macro and micro-texture measurements. In order to understand the evolved texture, the initial texture was modelled with the appropriate model using VPSC, and the micro-mechanism related to texture evolution has been demonstrated.

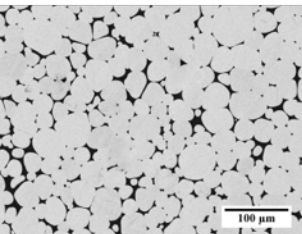
We believe this manuscript is appropriate for publication in MMTA. We have no conflicts of interest to disclose. Any correspondence related to the manuscript may kindly be communicated to me at [anishu@iitk.ac.in](mailto:anishu@iitk.ac.in).

Sincerely,

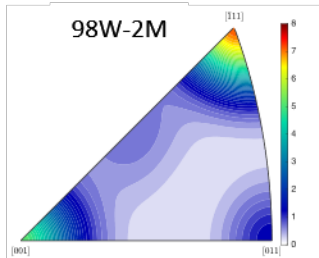
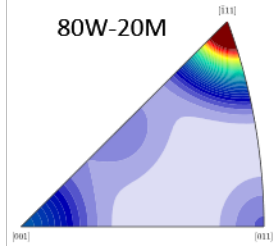
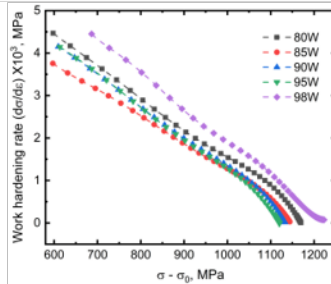
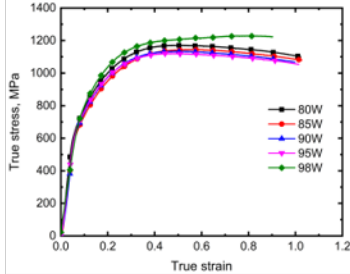
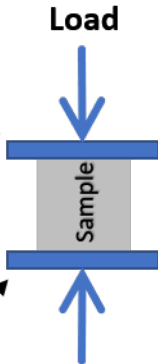
Anish Upadhyaya



80W-20M



98W-2M



# Effect of Tungsten Content and Compression on Microstructure and Texture Evolution in Liquid Phase Sintered Heavy Alloy

Mirtunjay Kumar, N.P. Gurao, Anish Upadhyaya\*

Department of Materials Science and Engineering,  
Indian Institute of Technology Kanpur 208016 INDIA

\* corresponding author: anishu@iitk.ac.in

## Abstract:

The crystallographic texture development in uniaxial compression tests of tungsten heavy alloys was systematically investigated by varying the tungsten content of the alloys. It was observed that a characteristic double fiber texture consisting of  $\langle 111 \rangle$  and  $\langle 100 \rangle$  fibers in the b.c.c. tungsten particles, regardless of the alloy composition under consideration. The effect of the composition was shown mainly in relation to the relative proportion of  $\langle 100 \rangle$  and  $\langle 111 \rangle$  fiber. It was observed that the  $\langle 100 \rangle$  fiber strengthens with increasing tungsten content, although the  $\langle 111 \rangle$  fiber remained as the strongest fiber in all the five compositions considered in the present work. The strengthening of  $\langle 100 \rangle$  fibers with an increased tungsten content was understood by performing self-consistent texture simulations in combination with a lattice corotation scheme to account for the role of neighboring grain orientations in texture evolution. A physical justification of the role of the neighbors is given by the shift of the orientations around the  $[110]$ - $[411]$  divergent line. The random fluctuations that originate from the neighbors displaces the orientation from the above of divergent downwards, which in turn leads to the displaced grains rotating in the direction of the  $\langle 100 \rangle$  corner.

**Keywords:** Tungsten heavy alloys; Texture; VPSC

## 1. Introduction

Tungsten Heavy Alloys (WHA) are widely used as kinetic-energy penetrators (KEP), vibration dampers, counterweights and medical radiation protection devices, due to their unique combination of characteristics such as high density (16-18 g/cm<sup>3</sup>) and strength (1000-1700 MPa), reasonably ductile (10-30%), excellent corrosion resistance and easy machinability <sup>[1]</sup>. Depleted uranium alloys have traditionally been used as KEP materials. However, because of their environmental and health concerns, there is a need to replace these alloys with an alternative material <sup>[2]</sup>. WHA are the most promising alloys in this regard and have therefore received a great deal of attention from many researchers in the past. Although the properties of WHAs are very promising, they lack a self-sharpening effect, which in turn leads to the formation of mushroom head on impact <sup>[3]</sup>. Much effort has been made to strategically process the WHA to enhance the ballistic performance of WHA through tailoring the composition <sup>[4,5]</sup>, heat treatment <sup>[6]</sup> and manufacturing methods such as solid-state sintering <sup>[7]</sup>, liquid phase sintering <sup>[8]</sup>, spark plasma sintering <sup>[9]</sup>, microwave sintering <sup>[10]</sup>, electrodeposition <sup>[11]</sup>, laser melting deposition <sup>[12]</sup> and selective laser melting <sup>[13]</sup>.

The WHA are mainly produced by powder metallurgy using liquid phase sintering (LPS). These composites typically contain 80-98 wt% W along with transition metals such as Ni, Fe, Cu and Co, etc. WHA with a tungsten content of less than 80% by weight leads to slumping during sintering and microstructural inhomogeneities and is therefore generally not used for commercial applications <sup>[14]</sup>. The microstructure of these alloys can be characterized by the presence of rounded tungsten grains dispersed in a low melting point ductile matrix phase. The microstructural properties of WHA, such as the grain size of tungsten particles, connectivity (average two-dimensional coordination number of tungsten particles), contiguity (relative proportion of the tungsten-tungsten interface in relation to the total interface) and

volume fraction of matrix, play an important role in controlling the deformation behavior [15,16].

Much research has been done in the past to investigate the mechanical properties and microstructure evolution of WHAs over the past few decades [17–19]. Jinglian et al. [20] examined the WHA with fine particle size and showed the better mechanical properties and the development of early shear band formation. Das et al. [21] showed that these alloys can withstand up to 70% of deformation without cracking even at 400°C. The deformation behavior also depends on the strain rate and the temperature and flow stress increases with increasing strain rate and decreasing test temperature [22,23]. Significant flow softening was a characteristic observation when the grain size of the alloy was reduced to a few micrometers [24]. Yu et al. [25,26] and Zhang et al. [25,26] investigated the hot extrusion of WHA alloys, which led to an improvement in ultimate tensile strength and hardness but a decrease in ductility.

In practice, the WHA alloys are mainly subjected to compression deformation. Therefore, most of the work in earlier studies has focused on understanding the deformation behavior under compression in relation to the mechanical properties (work hardening rate, strain rate sensitivity) [27]. However, the evolution of the crystallographic texture during uniaxial compression tests was not taken into account. It is known that the mechanical properties are considerably dependent on the crystallographic texture [28]. It was shown that an improvement in the mechanical properties can be achieved through suitable texture engineering. The relationship between processing, texture and mechanical properties is also missing in WHA for different phase fractions of tungsten. Therefore, it is of the utmost importance to systematically study the texture evolution during the uniaxial compression of WHA in order to understand the governing deformation mechanism. The texture evolution of single-phase b.c.c. has been extensively investigated by many researchers in the past [29,30]. However, very little information is available for two-phase alloys, particularly for WHA.

In this context, the aim of the present work is to carry out texture measurements of WHAs after uniaxial compression tests in order to understand the deformation behaviour. In addition to the microstructural characterization, to supplement the texture measurements, simulation studies with viscoplastic self-consistent simulations are carried out.

## 2. Experimental Details

In the present work, elemental powders with a purity of 99.99% were used as raw material for the synthesis of W-Ni-Fe based WHA. The composition of the WHA and the corresponding sample nomenclatures are listed in Table 1. The powders were mixed in a stoichiometric ratio and compacted into a cylindrical shape using hydraulic press at 300 MPa.

**Table 1** Composition of tungsten heavy alloy.

Alloy	W (wt.%)	Ni (wt.%)	Fe (wt.%)
80W-20M	80	14	6
85W-15M	85	10.5	4.5
90W-10M	90	7	3
95W-5M	95	3.5	1.5
98W-2M	98	1.4	0.6

The tungsten compact was then sintered in a tube furnace at 1773 K for 1 hour under a flowing hydrogen atmosphere. A sintered alloy was obtained which consisted of coarse tungsten particles surrounded by a completely wet matrix phase.

The sintered composites were then cut into cylindrical samples ( $\varnothing 6 \text{ mm} \times 4.8 \text{ mm}$ ), having a length to diameter ratio of 0.8 <sup>[31]</sup> for performing uniaxial compression testing using a universal testing machine (Biss India Pvt Ltd). The strain rate used during the compression tests was kept at  $10^{-3} \text{ s}^{-1}$ . The compression tests were performed up to a true strain ( $\epsilon$ ) of

0.693, which corresponds to a 50% reduction in height. The compression tests were repeated three times to ensure reproducibility. Stearic acid was applied to both ends of the samples to minimize the friction between the compression anvil and the sample. The deformed samples were then subjected to microstructural and textural characterization by electron backscatter diffraction (EBSD) and bulk texture measurements. In order to carry out the EBSD analysis, the samples were cut along the compression direction, while for the texture measurement samples were cut perpendicular to the compression direction. Fig. 1 shows the schematic of planes in which the EBSD and texture measurements were carried out.

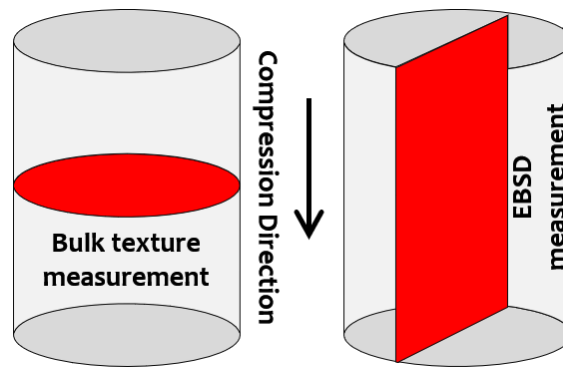


**Figure 1:** Schematic representing the planes for bulk texture by XRD and micro-texture by EBSD measurement.

The sectioned samples were initially polished to a mirror finish using the standard silicon carbide grit papers and alumina suspension. For EBSD, however, the samples were subjected to polishing with 0.04  $\mu\text{m}$  colloidal silica for an additional 30 minutes in order to obtain a strain-free surface. EBSD measurements were performed using a scanning electron microscope with a field emission gun operated (JEOL) at 20 kV voltage and 12 nA current. An Oxford Nordlys detector was used to collect EBSD data with a 0.5 $\mu\text{m}$  step size. The EBSD data were analyzed using commercially available TSL 8.0 software. Texture measurements were performed using a Rigaku four circle goniometer (Ultima IV). Four incomplete pole figures of tungsten b.c.c. phase namely (110), (200), (211), and (220) were measured with a maximum tilt angle of 70°. The orientation distribution function (ODF) was

then determined from the incomplete pole figures using the M-TEX software<sup>[32]</sup>. The ODFs were then used to calculate the inverse pole figures parallel to the direction of compression. It should be noted that due to the lower volume fraction of the matrix, the X-ray diffraction peaks associated with the f.c.c. Matrix were very weak. Therefore, the pole figure measurement of the f.c.c. Phase was not carried out. The texture measurement of the f.c.c. phase was done by performing large-scale EBSD maps.

### 3. Viscoplastic self-consistent Simulations

The viscoplastic self-consistent (VPSC) simulation predicts the texture evolution and the operative deformation mechanisms for different loading conditions, temperature and strain rates. Detailed information on the VPSC model can be found in the manual<sup>[33]</sup>. In the following section, however, the basics of the VPSC model and the simulation strategy chosen in this work are briefly explained. The grain level ( $\varepsilon_{ij}^g$ ) viscoplastic strain rate is related to local stress by a well-established constitutive law proposed by Hutchinson<sup>[33,34]</sup>.

$$\varepsilon_{ij}^g = \sum_s m_{ij}^s \gamma^s = \gamma_0 \sum_s m_{ij}^s \left( \frac{m_{kl}^s \sigma_{kl}^s}{\tau^s} \right)^{\frac{1}{m}} \quad (1)$$

Where,  $\gamma_0$  is the reference shear rate,  $m$  is the strain rate sensitivity,  $\tau^s$  is the critical resolved shear stress (CRSS) of the  $s^{th}$  slip system and  $m_{ij}^s$  is the symmetric Schmid tensor which can be written as

$$m_{ij}^s = \frac{1}{2} (\mathbf{n}_i^s \mathbf{b}_j^s + \mathbf{n}_j^s \mathbf{b}_i^s) \quad (2)$$

Where,  $\mathbf{n}$  is the slip plane normal and  $\mathbf{b}$  is the Burgers vector. The interaction between the ellipsoidal grain and HEM is defined by



$$(\varepsilon_{ij}^g - \bar{\varepsilon}) = -\tilde{M}(\sigma_{kl}^g - \bar{\sigma}) \quad (3)$$

Where,

$$\tilde{M} = n^{eff}(I - s^{-1}):S:\bar{M}^{sec} \quad (4)$$

Here,

Here,  $I$  and  $S$  represent the Identity and Eshelby tensor for a given grain. An adjustable parameter  $n^{eff}$  describes the nature of linearization for the compliance of the grain-matrix interactions [35]. The different values of  $n^{eff}$  implies the different nature of grain matrix interaction.  $n^{eff} = 0, 1, \sim 20$ , and  $\infty$  implies the Taylor, Secant, Tangent and Sachs model, respectively. The vicinity effect of two phases accounts a strong correlation in morphology and orientation between the grains. The 2-site self-consistent model, developed by Lebensohn and Canova [36], considers the two interacting grains of different phases deforming in the HEM [37]. The equations that correspond to VPSC-2S compared to the 1-site approach has been tabulated by Lebensohn et. al. [38].

The VPSC model includes hardening via the extended Voce hardening law. This law is based on the evolution of work hardening as a function of the accumulated shear strain in the grain [39].

$$\tau_c^\alpha = \tau_0^\alpha + (\tau_1^\alpha + \theta_1^\alpha \Gamma) \left[ 1 - \exp\left(-\frac{\theta_0^\alpha \Gamma}{\tau_1^\alpha}\right) \right] \quad (5)$$

Where,

$\Gamma = \sum_s |\Delta\gamma^s|$  is the total cumulative shear deformation by each active system  $s$  belonging to a slip mode  $\alpha$ .  $\tau_0^\alpha$ ,  $\theta_0^\alpha$ ,  $\tau_1^\alpha$ , and  $\theta_1^\alpha$  are the initial CRSS, initial hardening rate, back extrapolated CRSS and the asymptotic hardening rate, respectively. In the present work a VPSC-2S model [36] was used, which addresses the inclusion problem for a pair of grains embedded in the HEM. The two-phase model calculates one-site Eshelby tensors for the individual phases as well as two-site Eshelby tensors for each phase, which act as coupling

factors between the eigenstrain in one inclusion and the local deviation in strain of other phase<sup>[40]</sup>. Table 2 summarizes the Voce hardening parameters for a tungsten heavy alloy.

**Table 2** Parameters for extended Voce hardening law

Phase	Slip system family	$\tau_0$	$\tau_1$	$\theta_0$	$\theta_1$
W	$\{\bar{1}10\} < 111 >$	$\tau_0$	235	355	0
	$\{11\bar{2}\} < 111 >$	$1.3 \tau_0$	350	100	20
	$\{12\bar{3}\} < 111 >$	$1.5 \tau_0$	200	100	10
Matrix	$\{111\} < \bar{1}10 >$	$0.6 \tau_0$	200	100	0

The initial texture of the material (which is quite random, Fig. 2g) was taken as input and simulations were run up to a strain of 0.69 in 69 steps. Each simulation step corresponds to a strain increment of 0.01. It should be noted that the initial texture has been discretized to give 10,000 single orientations that will be used as input into VPSC. An aspect ratio of one was used for both the phases because the microstructures for both phases showed equiaxed grains.

## 4. Experimental Results

### 4.1. Initial microstructure and texture

The as-sintered microstructures of the two representative tungsten heavy alloys are shown in Fig. 2(a-b). The grain size of tungsten and the phase fraction of the matrix after sintering are listed in Table 3. A large standard deviation in grain size was observed due to the Ostwald ripening phenomenon during sintering. The phase fraction of the matrix was determined using the stereological area fraction method.

**Table 3:** Grain size and phase fraction of sintered WHA

Sample	Grain Size of W ( $\mu\text{m}$ )	Phase Fraction of Matrix
80W-20M	$21 \pm 8$	0.3
85W-15M	$20.7 \pm 8.4$	0.23
90W-10M	$22 \pm 7.2$	0.19
95W-5M	$20.2 \pm 7.3$	0.13
98W-2M	$20 \pm 5$	0.08

The alloys 80W-20M and 98W-2M were chosen because they represent the extreme conditions. Both the microstructures can be characterized by the presence of coarse tungsten particles surrounded by a fully wetting matrix. It can also be seen that contiguity, the W-W contact fraction, and the connectivity increases with the W content. Elemental distribution maps were also obtained via EDS to confirm the composition of the particles and the matrix. The brighter phase consisted of pure W and the darker phase consisted of solid solution Ni-24W-22Fe. The X-ray diffraction pattern shown in Fig. 2f confirms that the sample is free of any strain heterogeneity or size effects, as can be seen from the relatively sharp peaks with a small broadening (full width at half maximum). Aside from the peaks of the b.c.c. phase, a few small peaks corresponding to the f.c.c. phase can also be observed. The presence of a preferred orientation or crystallographic texture was also verified by measurement of bulk texture of the initial sample. The crystal orientation or inverse pole figure map along the compression direction shown in Fig. 2g suggests that the texture in the initial sample is random. It should be noted that texture measurements were undertaken for all five samples. However, for brevity, the IPF||CD of only 80W-20M is shown. It was also observed that the texture of the other compositions was random.

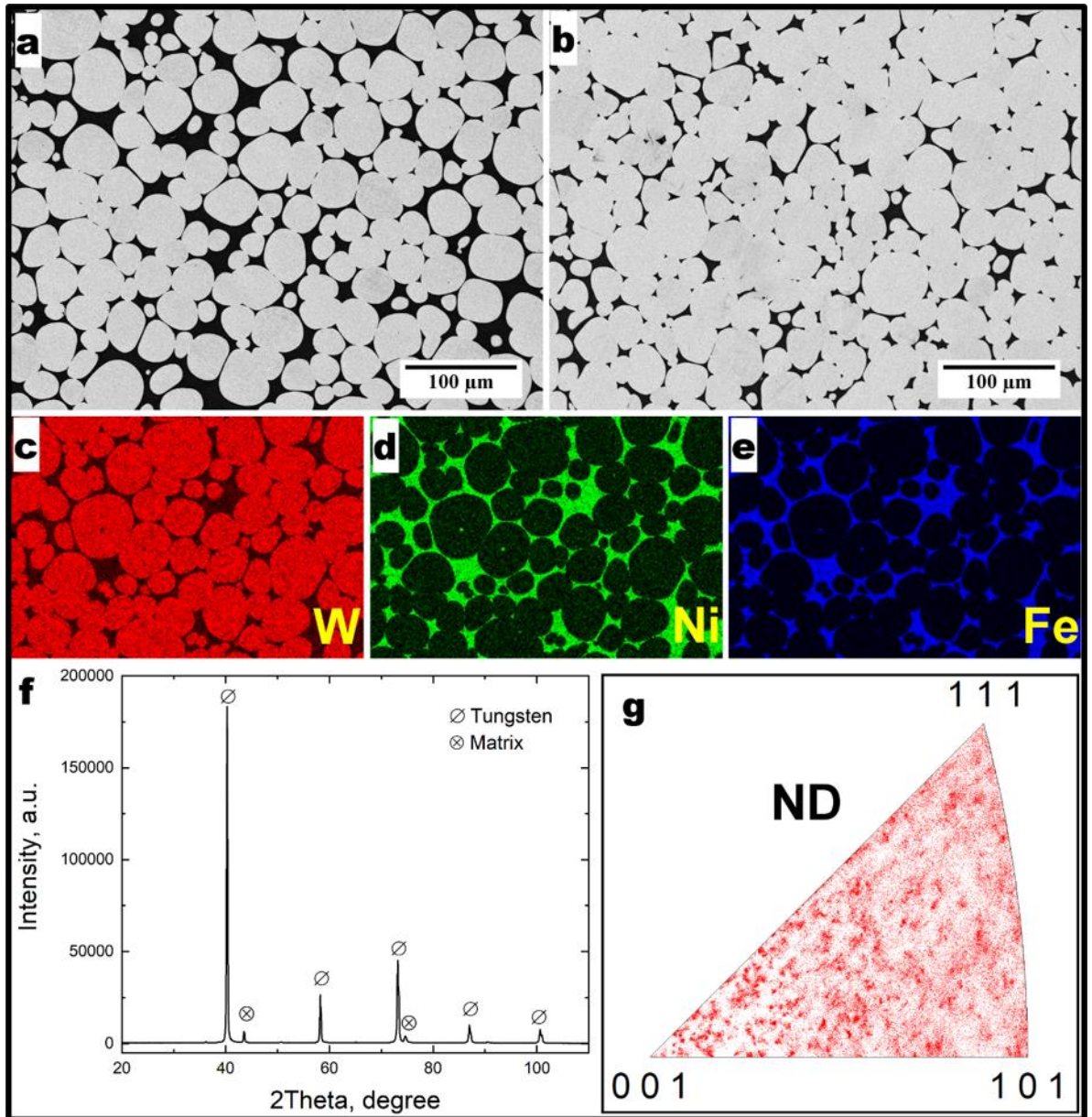


**Figure 2:**(a) Backscattered electron images for 80W-20M alloy (b) Backscattered electron images for 98W-2M alloy (c-e) elemental distribution maps by EDS (f) x-ray diffractogram for 80W-20M alloy (g) Inverse pole figure plotted parallel to the compression direction for 80W-20M alloy

## 4.2. Texture evolution of tungsten heavy alloy during uniaxial compression

Figure 3 shows the true stress - true strain curve and work hardening rate  $\left(\frac{d\sigma}{d\varepsilon}\right)$  vs  $\sigma - \sigma_0$  for all the alloys. All the sample behaved in similar manner and the dominance of the stage III deformation<sup>[41]</sup> was evident as a straight line in work hardening curve.

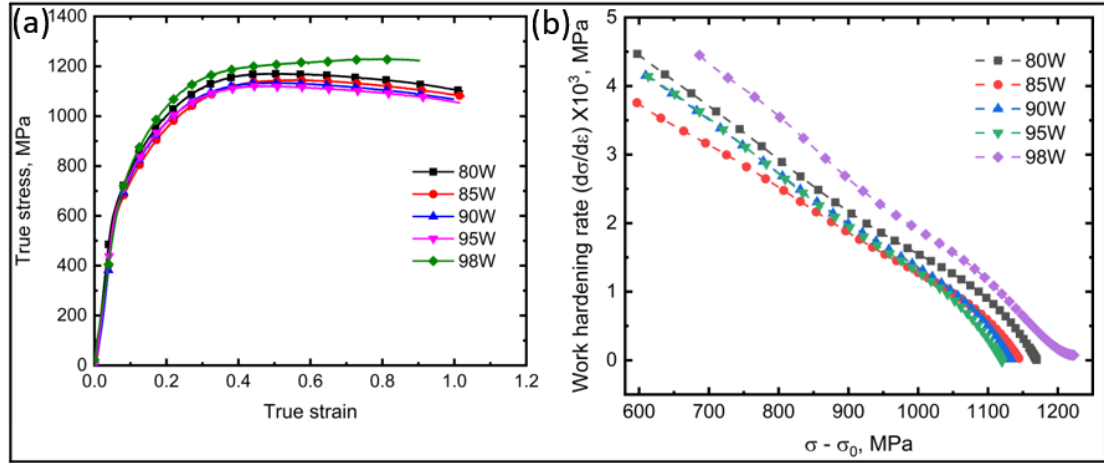


**Figure 3:**(a) True stress-true strain plot of WHAs (b) Work hardening rate vs  $\sigma - \sigma_0$  of WHAs

Figure 4a shows the IPF<sub>||</sub>CD (compression direction) for all the five alloy compositions considered in the present work. As can be observed, the classical double-fiber texture with weak  $\langle 100 \rangle$  fiber and major  $\langle 111 \rangle$ ||CD fiber is obtained after uniaxial compression. This is the typical texture found in many b.c.c. metals and alloys after uniaxial compression. However, a closer look at the IPF's suggests that there is a systematic influence of the composition on the texture evolution, mainly with regard to the relative proportion of  $\langle 100 \rangle$  and  $\langle 111 \rangle$  fibers. This behavior is elegantly shown in Fig. 4d where the ratio of the volume fraction of  $\langle 100 \rangle$  and  $\langle 111 \rangle$  fibers is plotted. It can be clearly seen that the volume fraction ratio increases with increasing tungsten content. The volume fraction of the individual fibers is also shown in Fig. 4c. Although the  $\langle 111 \rangle$  fiber is the strongest for all of the present compositions, it is apparent that the volume fraction of  $\langle 100 \rangle$  fiber increases steadily with an increase in the tungsten content. As already mentioned, texture measurements via XRD were

not possible for the f.c.c phase because of very weak peaks (Fig. 2f). Therefore, the texture measurement of the matrix phase was carried out via EBSD. Fig. 4b shows inverse pole figure for the f.c.c. phase in the compression direction. It can be seen that the classical  $\langle 110 \rangle \parallel \text{CD}$  texture evolves after uniaxial compression up to a height reduction of 50%. The texture of the f.c.c. phase is quite weak (2.5 mrd) compared to the main tungsten phase (8.0 mrd). This weak texture can be attributed to the relatively lower volume fraction of the f.c.c. phase compared to the b.c.c. phase. Therefore, in the following we will concentrate entirely on the texture development of the b.c.c. tungsten phase, with reference to the f.c.c. matrix phase wherever this is required.

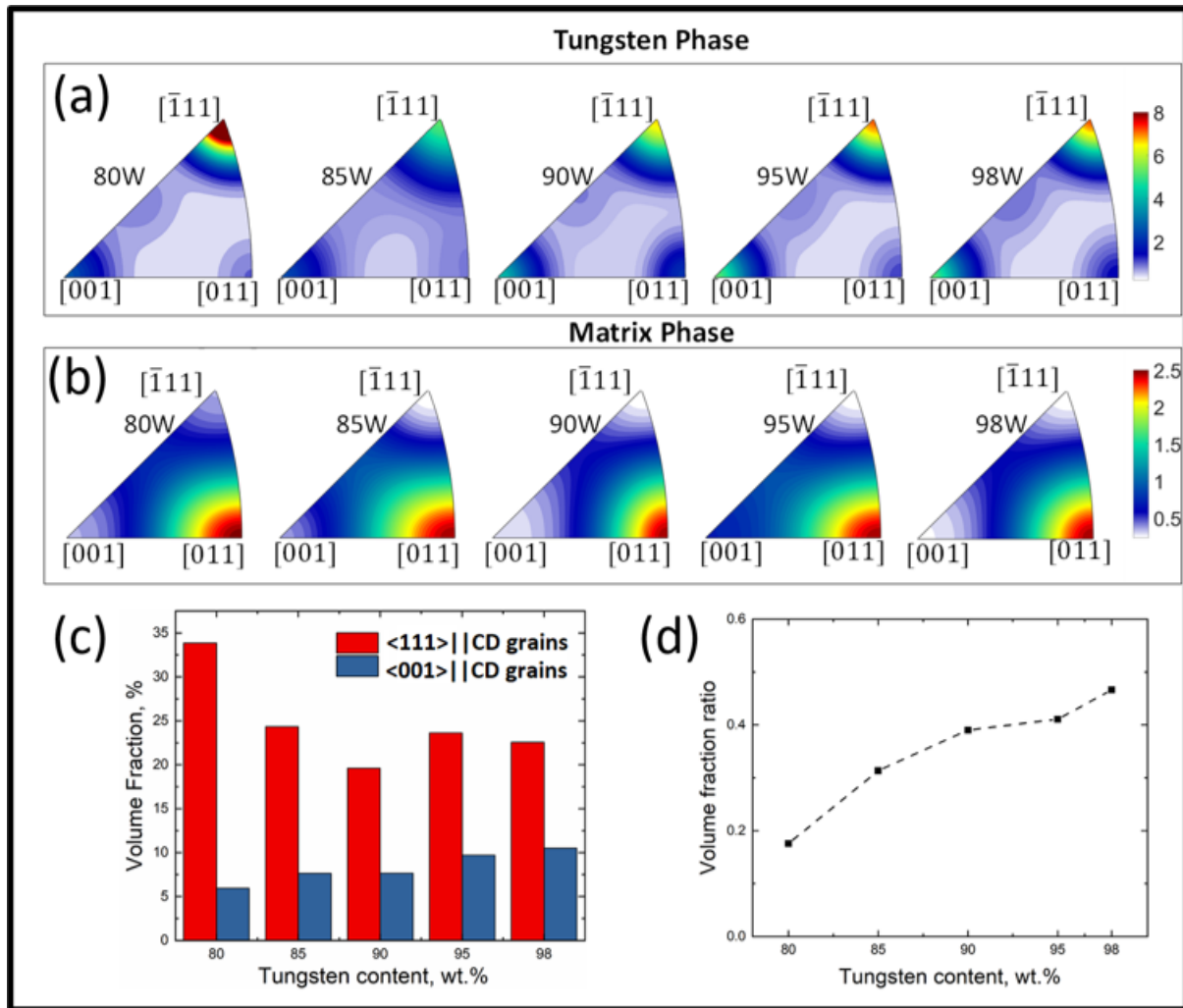


**Figure 4:**(a-b) Inverse pole figures plotted parallel to compression direction for different composition of tungsten and matrix (c) volume fractions of  $\langle 111 \rangle$  and  $\langle 100 \rangle$  fibre for



different composition (d) volume fraction ratio of  $\langle 100 \rangle$  to  $\langle 111 \rangle$  fibre as a function of tungsten content.

#### 4.3. Microstructural evolution during uniaxial compression of tungsten heavy alloy

The inverse pole figure maps and phase maps of the deformed tungsten heavy alloys are shown in Fig. 5a and 5b, respectively. The color code to represent the grain orientations is shown in Fig. 5e. The compression direction (CD) is marked in the IPF maps. The maps clearly show the orientation gradient in the microstructure, which means a heterogeneous deformation.

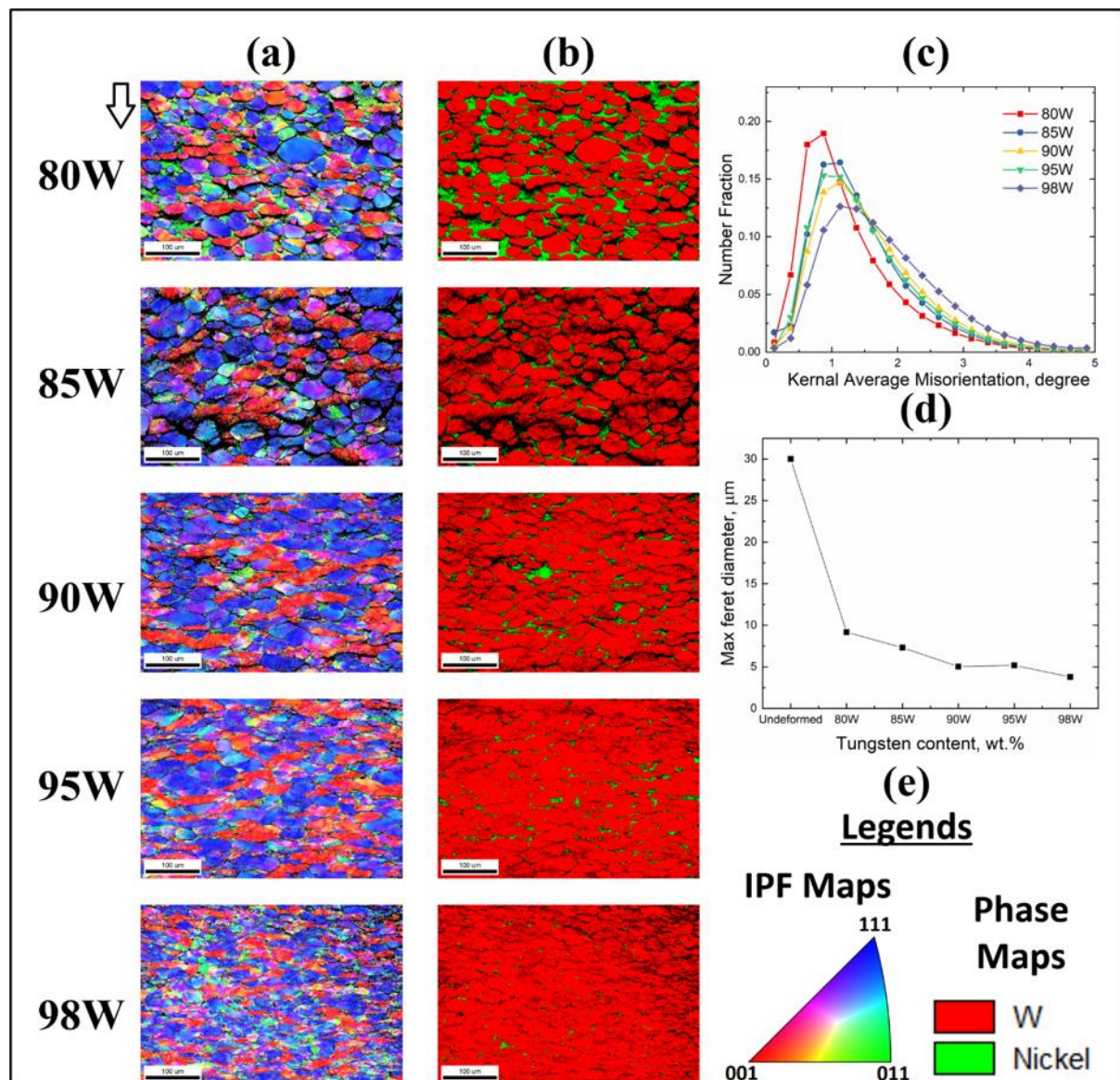


**Figure 5:** (a-b) Inverse pole figure maps plotted parallel to compression direction and phase maps for different compositions, respectively. (c) Kernel average misorientation distribution profiles. (d) Feret diameter as a function of tungsten content. (e) IPF color key.

The presence of an intragranular orientation gradient is common in deformed microstructures and depends on the initial orientation as well as neighboring grains. In addition, deformation banding can be observed in the microstructures which can lead to fragmentation of grains. Apart from these general characteristics, there is also a systematic influence of the composition on the development of the microstructure. As can be observed, the extent of the strain heterogeneity of the tungsten phase increases with increasing tungsten content. This heterogeneity can be attributed to the strain partitioning effect between the soft matrix phase and the hard tungsten phase. With an 80W-20M alloy, the matrix can accommodate a significant amount of imposed deformation compared to the 98W-2M alloy, where the matrix volume fraction is minimal. With the 98W-2M alloy, the tungsten phase must accommodate most of the deformation imposed. This is elegantly captured by the aspect ratio of the tungsten particles, where the particles in the 80W-20M alloy are relatively equiaxed compared to 98W-2M alloy, where the particles have developed a pancake shape and are elongated in the radial direction. The Kernel Average Misorientation (KAM) plot (Fig. 5c) also confirms this observation. The KAM represents the average misorientation of a pixel with its neighboring pixels and is therefore ideally suited for estimating the strain heterogeneity. Fig. 5c indicates that the KAM distribution of tungsten particles shifts to higher angles with increasing tungsten content. This confirms our argument that the dislocation activity and strain heterogeneity of the tungsten particles is a strong function of the matrix content. Additional evidence of this behavior is obtained from the Feret diameter of the particles. The Feret diameter corresponds to the greatest distance between the two parallel lines on the opposite side of randomly oriented particles. Therefore, a reduction in the



Feret diameter is an indication of a reduction in grain size and grain fragmentation of tungsten particles. As can be seen in Fig. 5d, the Feret diameter is the smallest for the 98W-2M alloy. After analyzing the phase-dependent deformation, we now shift our attention to the orientation-dependent deformation of tungsten particles. The tungsten particles constitute the major portion of these alloys and therefore require further investigation of their deformation behavior. In this regard, the two orientations correspond to the major texture components i.e.,  $\langle 100 \rangle$  and  $\langle 111 \rangle \parallel \text{CD}$  were partitioned with a tolerance angle of  $10^\circ$ .

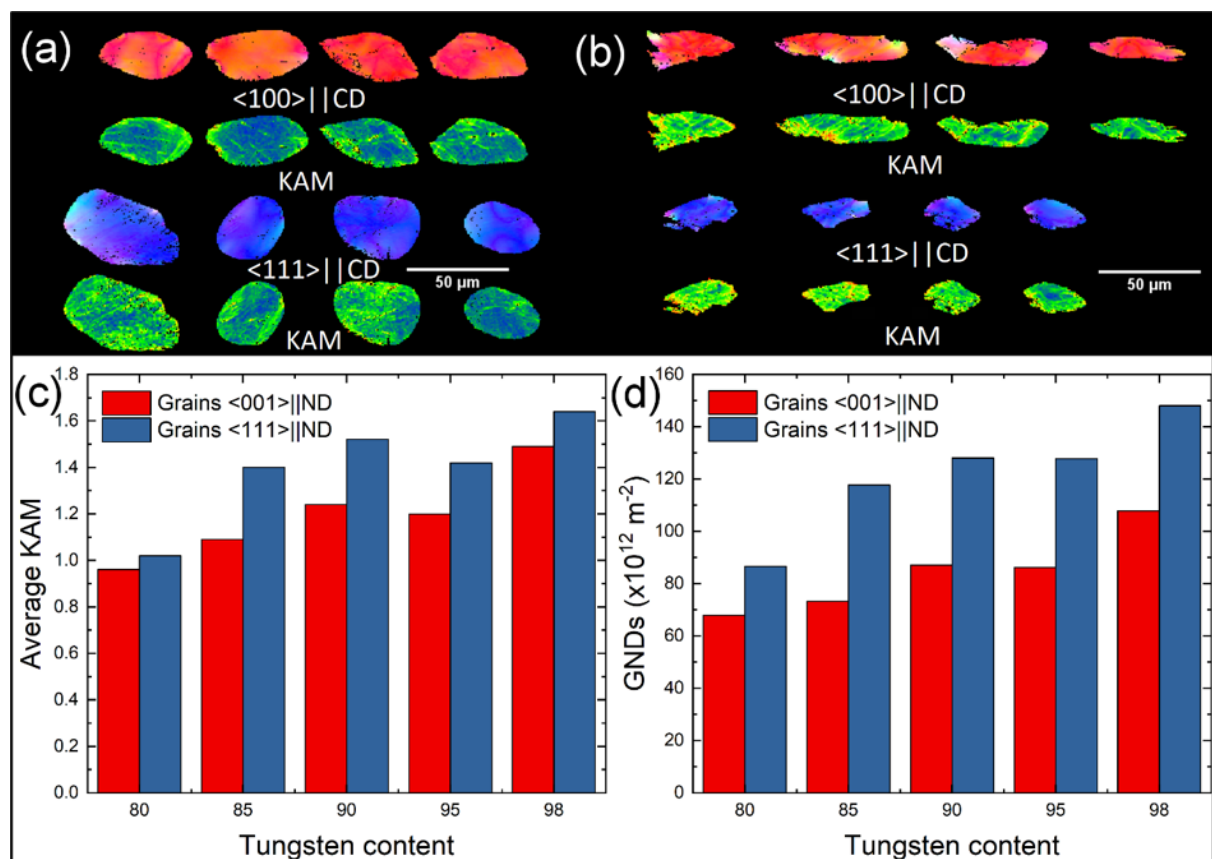


**Figure 6:** (a-b) Set of grains representing  $\langle 111 \rangle$  and  $\langle 100 \rangle$  fibers with their KAM map for 80W-20M and 98W-2M, respectively. (c-d) KAM and GND histogram as the function of tungsten content.

Figure 6(a-b) highlights some representative grains of the  $\langle 100 \rangle$  and  $\langle 111 \rangle$  orientations. As before with the strain partitioning between the phases, we call up the KAM again to analyze

the deformation behavior of  $\langle 100 \rangle$  and  $\langle 111 \rangle$  oriented grains. As can be observed in Figure 6c, the average KAM for  $\langle 111 \rangle$  oriented grains compared  $\langle 100 \rangle$  oriented grains is higher regardless of the alloy composition. However, the difference between the KAM values increases as the tungsten content increases. This can be explained by the higher strain accommodation of tungsten particles with increasing tungsten content. A simplified explanation of the higher KAM value of  $\langle 111 \rangle$  oriented grains compared to  $\langle 100 \rangle$  oriented grains can be provided with regard to the Taylor factor. As calculated for axisymmetric deformation, the Taylor factor is 3.67 for  $\langle 111 \rangle$  oriented grains compared to 2.44 for  $\langle 100 \rangle$  oriented grains. Therefore, more work or plastic shearing is required in the  $\langle 111 \rangle$  grains in order to achieve the same equivalent strain compared to  $\langle 100 \rangle$  grains. This also increases the dislocation activity in  $\langle 111 \rangle$  grains higher compared to  $\langle 100 \rangle$  grains on the microscopic length scale, which leads to the formation of dislocation boundaries, which in turn lead to a higher KAM. The geometrically necessary dislocation density (Fig. 6d) for the two grain families also confirms our arguments.

## 5. Simulation results

As mentioned earlier, VPSC was used to perform texture simulations. It is known that the texture evolution in b.c.c. metals and alloys can be attributed to pencil glide on  $\{110\}$ ,  $\{112\}$  and  $\{123\}$  slip planes with the common  $\langle 111 \rangle$  slip direction<sup>[42]</sup>. Therefore, we also selected pencil glide in VPSC for performing texture simulations. Based on a comparison between experimental and simulated texture, it was found that another important aspect to decide before executing the VPSC code is the deformation mode. The VPSC code allows the  $n^{eff}$  parameter to be tuned to mimic the two extremes of plastic deformation viz. the upper bound Taylor type and the lower bound Sachs type. As can be seen from equation 6,  $n^{eff} = 0$  corresponds to a Taylor type deformation, while  $\infty$  corresponds to Sachs type deformation. Since the mode of deformation is unknown in advance, we performed texture simulations

313 taking into account the different modes and based on the agreement between experimental  
314 and simulation results, the mode of deformation is determined. It should be noted that  
315  $n^{eff}=100$  is enough to simulate the Sachs-type deformation behavior as it is physically  
316 impossible to use infinity in the VPSC code. Other key parameters required to run the VPSC  
317 simulations such as the velocity gradient, total strain imposed, and strain increment are  
318 specified in section 3. It has been observed that secant type deformation with simultaneous  
319 rotation of adjacent grains adequately reproduces the experimental results. This can be  
320 justified physically with the requirement of strain compatibility at the tungsten-tungsten and  
321 tungsten-matrix interface and the equiaxed nature of the tungsten particles. It is also generally  
322 accepted that strain compatibility is a more important criterion than stress compatibility  
323 (Sachs mode) during plastic deformation. In Fig. 2(a-b), it can be observed that the contact  
324 between tungsten-tungsten particles is much more prevalent in the 98W alloy than in 80W  
325 alloy. It is known that neighboring orientations can significantly change the local velocity  
326 gradient compared to the macroscopically imposed velocity gradient, which in turn can lead  
327 to completely different rotation paths and thus final texture <sup>[43]</sup>. In the VPSC model, the  
328 influence of neighbors can be taken into account in an empirical way by randomly pairing the  
329 grains, which are then caused to co-rotate. The co-rotation scheme was used in the VPSC 7D  
330 model by Tomé et al. <sup>[44]</sup>. This scheme leads to a different rotation path for similarly oriented  
331 grains based on the chosen neighbor. As can be seen from Fig. 2(a-b), a single tungsten  
332 particle is in contact with an average of five other particles for the 98W alloy compared to  
333 two for the 80W alloy. Therefore, random pairs of five and two particles were considered for  
334 performing texture simulations of 98W and 80W alloy, respectively.

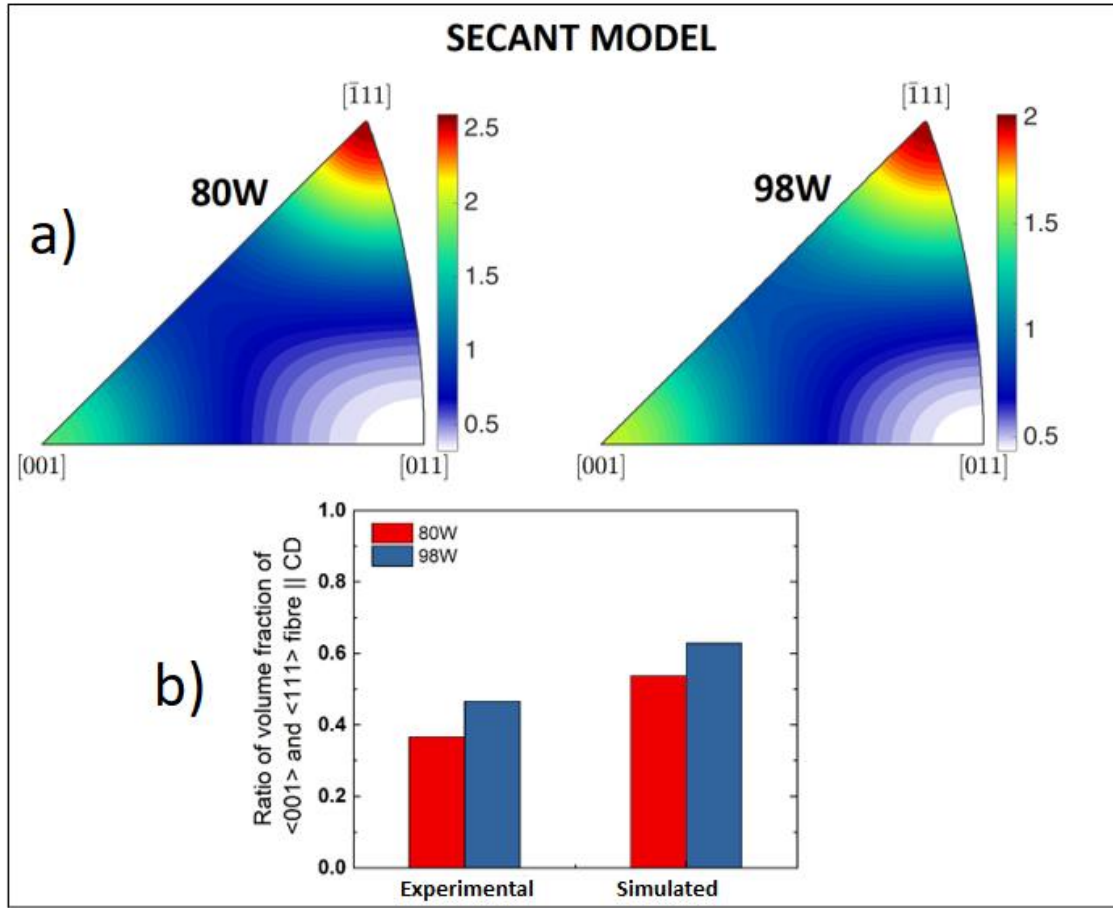


**Figure 7:** (a) Predicted inverse pole figure (IPF) parallel to compression direction by Secant model for the two extreme compositions considering the connectivity of the tungsten particles. (b) Comparison between experimental and simulated ratios of volume fraction of <100> and <111> fibres.

Fig. 7 shows the simulated inverse pole figures together with the comparison between the experimental and the simulated volume fraction ratio. It can be said that the agreement between experimental and simulation results matches significantly in agreement when the grains are paired and rotated together. The intensity near the <100> corner is clearly high for the 98W-2M alloy compared to the 80W-20M alloy. The simulated volume fraction ratio of the two alloys also follows a trend similar to that observed experimentally. Although this is a simplified way of looking at the effect of neighboring particles, it underlines their role in plastic deformation and the resulting texture development. It should be noted that all of these

VPSC simulations were performed with considering the two-phase scenario i.e., VPSC-2S model. The phase fraction was suitably set in VPSC depending upon the alloy composition. Thus, in addition to the texture of the tungsten particles, the simulated texture of the matrix was also obtained. Fig. 8(a-b) shows the inverse pole figure in the compression direction, the classic  $\langle 110 \rangle$  fiber texture during f.c.c compression is satisfactorily reproduced by VPSC simulations. The activity diagrams showing the strain partitioning and the average active systems per grain (AVACS) between the two phases are shown in Figure 8b.

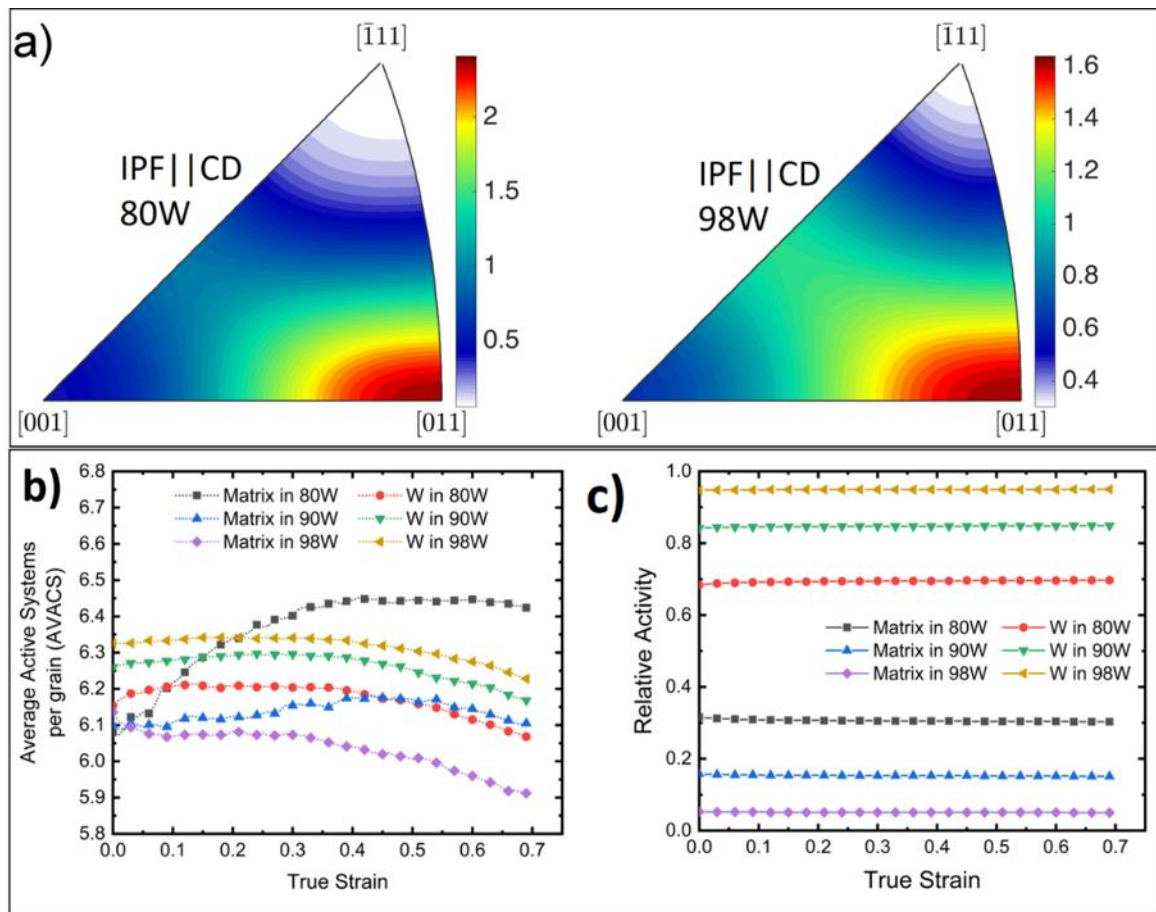


**Figure 8:** (a) Inverse pole figure (IPF) parallel to compression direction predicted by Secant model for matrix for the two-extreme composition. (b) Strain partitioning represented by the relative activity of the slip systems as a function of true strain. (c) Predicted average active slip systems per grain as a function of true strain.

On average, six slip systems were active and showed a deformation close to the upper bound model in all the alloy. The tungsten particles, which are the dominant phase, bear most of the externally imposed deformation compared to the matrix phase, so that the relative activity (shown in Fig. 8c) of tungsten is always higher than that of the matrix.

## 6. Discussion

The texture evolution during compression can be fully understood by showing the lattice rotation behavior in an inverse pole figure. A schematic representation of the lattice rotation is shown in Fig. 9a.

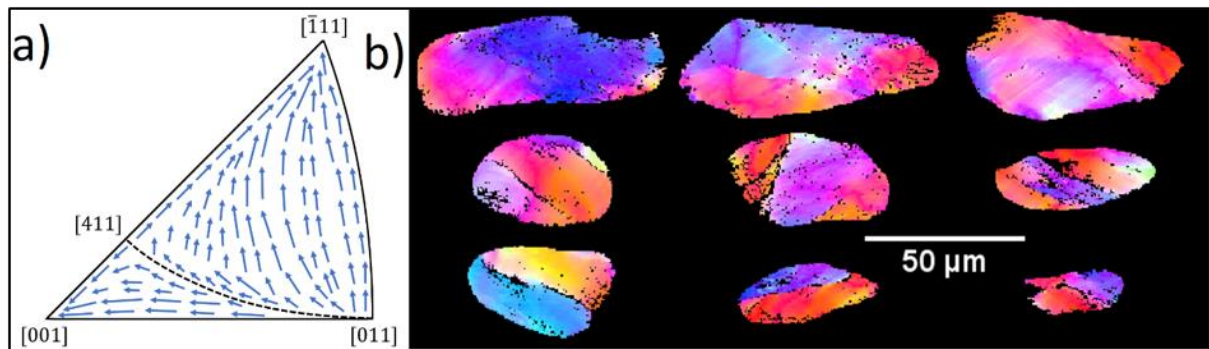


**Figure 9:** (a) Schematic of lattice rotation during uniaxial compression for b.c.c. (b) Representative grains showing the orientations lying on both side of divergent line in a single grain.

The lattice rotation path was obtained by Rosenberg and Piehler<sup>[45]</sup> by implementing the pencil-glide hypothesis. As can be seen, the grains tend to rotate in direction  $\langle 111 \rangle$  or  $\langle 100 \rangle$  depending upon the orientation of the compression axis. All the grains lying above the  $[110]$ - $[411]$  line would rotate towards  $\langle 111 \rangle$ , whereas the grains lying below the  $[110]$  -  $[411]$  line would rotate in the direction of  $\langle 100 \rangle$ . The  $[110]$  -  $[411]$  line is generally known in the literature as ‘divergent line’<sup>[46]</sup>. For an initial random texture, a majority of the grains would be lying above the divergent line compared to the one below. As a result, a large proportion of the grains would come close to  $\langle 111 \rangle$  compared to  $\langle 100 \rangle$ . Rosenberg and Piehler<sup>[47]</sup>

383 calculated using simulations that for an initial random texture 74% of the grains would rotate  
384 in the direction of  $\langle 111 \rangle$ , compared with 26% in the direction  $\langle 100 \rangle$ . This explains the  
385 experimental observation of the relative dominance of  $\langle 111 \rangle$  fibers compared to  $\langle 100 \rangle$   
386 fibers, regardless of alloy composition. It should be noted that the above rotational paths were  
387 predicted without considering the influence of neighboring grains. As has been discussed by  
388 several researchers in the past, the deformation behavior of individual grains depends heavily  
389 on their neighborhood. The local state of stress within the individual grains can, depending on  
390 the environment, deviate significantly from the macroscopic imposed deformation, which in  
391 turn influences the selection of active slip systems and thus the lattice reorientation.  
392 However, the determination of the local stress state is not easy and requires high precision  
393 measurements of the elastic strains in relation to internal stresses using high-resolution EBSD  
394 <sup>[48]</sup>. Otherwise, three-dimensional in-situ diffraction experiments with high-energy X-rays and  
395 neutrons that can penetrate deep into the crystals are required to measure the full elastic strain  
396 tensor for several individual grains. Even with such high-end experiments, the best approach  
397 to determining the exact state of stress is still being discussed in the literature. Therefore, we  
398 will only make a qualitative attempt to understand the role of the local neighborhood in the  
399 texture evolution. In the present work the effect of the local neighborhood manifests itself in  
400 the form of an increasing volume fraction ratio of  $\langle 100 \rangle$  and  $\langle 111 \rangle$  fibers with increasing  
401 tungsten content. As previously demonstrated via VPSC, running Secant simulations without  
402 considering the neighboring orientations did not provide a satisfactory match to the  
403 experimental texture, particularly for the 98W-2M alloy. Only when texture simulations were  
404 performed by pairing five randomly oriented grains, a reasonable match was reached. A clear  
405 picture of the role of the neighbors can be obtained from the lattice rotation schematic in Fig.  
406 9a. It can be considered that the orientations that are close to the deviation line follow rather  
407 unpredictable rotation paths compared to orientations that are far away from the deviation

408 line. A slight fluctuation due to the local neighborhood can lead to the orientation being  
409 shifted from above the divergence line downwards and vice-versa. As a result, the grain will  
410 now follow completely new rotation path compared to the path it should take based on its  
411 initial orientation. On the other hand, the grains that are far from the divergent line can pick  
412 up small random fluctuations due to the neighbors and continue to follow the predicted path  
413 of rotation, albeit at reduced speeds. Looking at the initial random texture in the present case,  
414 where a large proportion of grains lie above the divergent line, it can be said that a greater  
415 number of grains make the transition from above the divergent line to the bottom and not vice  
416 versa. Subsequently, these grains then rotate in direction  $\langle 100 \rangle$  compared to  $\langle 111 \rangle$ . The  
417 rotation in the  $\langle 100 \rangle$  direction is also energetically favourable since the Taylor factor is  
418 steadily decreasing<sup>[49]</sup>. It is known that grains with a lower Taylor factor are considered to be  
419 ‘soft grains’ in which the imposed deformation can be easily accommodated, compared to  
420 ‘hard grains’ with a higher Taylor factor. The hard grains develop more deformation  
421 heterogeneities compared to the soft grains and are therefore more sensitive to the local  
422 neighborhood. For a 98W-2M alloy, where contact between tungsten-tungsten particles is  
423 significant, the fluctuations are more frequent than for an 80W-20M alloy, where the contact  
424 between tungsten-tungsten particles is limited. As a result, the 80W-20M alloy will follow  
425 the predicted lattice rotation paths and develops a significantly stronger  $\langle 111 \rangle$  fiber  
426 compared to the  $\langle 100 \rangle$  fiber. On the other hand, the 98W-2M alloy develops a stronger  
427  $\langle 100 \rangle$  fiber with high probability of fluctuations. Further confirmation of our arguments can  
428 be obtained from EBSD measurements. As previously shown, the deformation heterogeneity  
429 is significantly higher for the 98W-2M alloy compared to the 80W-20M alloy. The amount of  
430 grain fragmentation, shown in terms of Feret diameter, is also higher for the 98W-2M alloy.  
431 All of these effects can be attributed to unforeseen rotation paths in the 98W-2M alloy due to  
432 the local neighborhood, which prevents homogenous deformation of the grain as a whole.



Different parts of the same grain deform via different slip systems, which leads to the development of a strong orientation gradient and ultimately to fragmentation. Some representative grains are shown in Fig. 9b where it can be observed that one part of the grain is above the divergence line while the other is below it. This supports our argument that a higher probability of fluctuations could be the determining factor for a stronger  $\langle 100 \rangle$  fiber in the 98W-2M alloy. Other theories of texture evolution such as the changing the mode of deformation from Taylor-type to Sachs-type to explain the strengthening of  $\langle 100 \rangle$  fiber is not applicable since Sachs deformation results in an inappropriately strong  $\langle 100 \rangle$  fiber, this is not observed experimentally. The overall texture is still dominated by  $\langle 111 \rangle$  fibers, although the random fluctuations slightly increase the volume fraction of  $\langle 100 \rangle$  fibers. Also, the role of strain rate sensitivity, which is sometimes used in the texture community, is limited here because the deformation was performed at room temperature and at nominal strain rates. Therefore, it can be said that the shift in orientations along the divergent line due to local neighborhood provides a reasonable explanation for the texture evolution of b.c.c. tungsten particles. The texture evolution of the matrix phase can again be understood by the schematic shown in Fig. 9a. Since the slip systems in f.c.c. have their planes and directions interchanged with respect to b.c.c., one can say that the direction of rotation is opposite to that shown in the schematic diagram. In this case, the grains aggregate in the vicinity of  $\langle 110 \rangle$  and the divergent line behaves like a convergent line. Since the grains tend to rotate in direction  $\langle 110 \rangle$  regardless of their initial orientation, the role of local neighborhood or random fluctuations during f.c.c compression is limited.

## 7 Summary

In the present work a uniaxial compression test was carried out in order to understand the deformation mechanisms and the texture evolution of tungsten heavy alloys. The most important findings of the present work are summarized below.

1. The texture evolution of the b.c.c. tungsten particles can be characterized by the development of  $\langle 111 \rangle + \langle 100 \rangle$  double fiber texture, whereas a  $\langle 110 \rangle$  fiber evolved in the f.c.c. matrix phase. The effect of composition is manifested in terms of relative proportion of  $\langle 100 \rangle$  and  $\langle 111 \rangle$  fibers where the volume fraction ratio of  $\langle 100 \rangle$  and  $\langle 111 \rangle$  fibers increase with increasing tungsten content.
2. Texture simulations via VPSC suggested that a secant type deformation pattern was followed in the WHA instead of the Sachs-type deformation. However, Secant-type deformation combined with the lattice corotation scheme to include the effect of neighboring orientations was essential to correctly reproduce the experimental textures. A five-grain pair was used for the 98W-2M alloy, while a two-grain pair was used for the 80W-20M alloy to run the simulations.
3. The physical interpretation of the role of neighbors in increasing the  $\langle 100 \rangle$  fiber is provided in view of a high probability of fluctuations in the 98W-2M alloy leading to a shift in orientations from above the  $[110]$ - $[411]$  divergent line to below it and the subsequent rotation in the direction of the  $\langle 100 \rangle$  corner.

## Acknowledgement

The authors thank the powder metallurgy lab, texture lab and ACMS IIT Kanpur for facilitating texture and EBSD measurements.

## Conflict of Interest

The authors have not conflict of interest to declare.

## Data Availability statement

Data will be made available on request

481 **References:**

- 482 1 Y. Li, K. Hu, X. Li, X. Ai, and S. Qu: *Materials Science and Engineering: A*, 2013, vol.  
483 573, pp. 245–52.
- 484 2 A. Upadhyaya: *Materials Chemistry and Physics*, 2001, vol. 67, pp. 101–10.
- 485 3 R. Luo, D. Huang, M. Yang, E. Tang, M. Wang, and L. He: *Materials Science and*  
486 *Engineering: A*, 2016, vol. 675, pp. 262–70.
- 487 4 A. Bose, R. Sadangi, and R.M. German: *Supplemental Proceedings: Materials*  
488 *Processing and Interfaces*, 2012, vol. 1, pp. 453–65.
- 489 5 U.R. Kiran, A. Panchal, M. Sankaranarayana, G.V.S.N. Rao, and T.K. Nandy:  
490 *Materials Science and Engineering: A*, 2015, vol. 640, pp. 82–90.
- 491 6 U.R. Kiran, A.S. Rao, M. Sankaranarayana, and T.K. Nandy: *International Journal of*  
492 *Refractory Metals and Hard Materials*, 2012, vol. 33, pp. 113–21.
- 493 7 W.E. Gurwell: *MATERIAL AND MANUFACTURING PROCESS*, 1994, vol. 9, pp.  
494 1115–26.
- 495 8 U.R. Kiran, A. Panchal, M. Sankaranarayana, and T.K. Nandy: *International Journal of*  
496 *Refractory Metals and Hard Materials*, 2013, vol. 37, pp. 1–11.
- 497 9 L. Ding, D.P. Xiang, Y.Y. Li, C. Li, and J.B. Li: *International Journal of Refractory*  
498 *Metals and Hard Materials*, 2012, vol. 33, pp. 65–9.
- 499 10 A. Mondal, A. Upadhyaya, and D. Agrawal: *International journal of refractory metals*  
500 *and hard materials*, 2010, vol. 28, pp. 597–600.
- 501 11 F. He, J. Yang, T. Lei, and C. Gu: *Applied surface science*, 2007, vol. 253, pp. 7591–  
502 8.
- 503 12 C. Li, S. Ma, X. Liu, J. Li, and G. Le: *International Journal of Refractory Metals and*  
504 *Hard Materials*, 2018, vol. 77, pp. 113–9.
- 505 13 A. Iveković, M.L. Montero-Sistiaga, K. Vanmeensel, J.-P. Kruth, and J. Vleugels:  
506 *International Journal of Refractory Metals and Hard Materials*, 2019, vol. 82, pp. 23–  
507 30.
- 508 14 A. Upadhyaya and R.M. German: *Metallurgical and Materials Transactions A*, 1998,  
509 vol. 29, pp. 2631–8.
- 510 15 D.-K. Kim, S. Lee, and H. Song: *Metallurgical and Materials transactions A*, 1998, vol.  
511 29, pp. 1057–69.
- 512 16 Z. Wei, J. Yu, S. Hu, and Y. Li: *International journal of impact engineering*, 2000, vol.  
513 24, pp. 747–58.
- 514 17 N.K. Çalışkan, N. Durlu, and Ş. Bor: *International Journal of Refractory Metals and*  
515 *Hard Materials*, 2013, vol. 36, pp. 260–4.
- 516 18 N. Senthilnathan, A.R. Annamalai, and G. Venkatachalam: *Materials Science and*  
517 *Engineering: A*, 2018, vol. 710, pp. 66–73.
- 518 19 S. Yadav and K.T. Ramesh: *Materials Science and Engineering: A*, 1995, vol. 203,  
519 pp. 140–53.
- 520 20 F. Jinglian, G. Xing, Q. Meigui, L. Tao, L. Shukui, and T. Jiamin: *Rare Metal Materials*  
521 *and Engineering*, 2009, vol. 38, pp. 2069–74.
- 522 21 J. Das, G.A. Rao, S.K. Pabi, M. Sankaranarayana, and B. Sarma: *Materials Science*  
523 *and Engineering: A*, 2011, vol. 528, pp. 6235–47.
- 524 22 W.-S. Lee, C.-F. Lin, and S.-T. Chang: *Journal of Materials Processing Technology*,  
525 2000, vol. 100, pp. 123–30.

526 23 W.-S. Lee, G.-L. Xiea, and C.-F. Lin: *Materials Science and Engineering: A*, 1998, vol.  
527 257, pp. 256–67.

528 24 Q. Wei, T. Jiao, K.T. Ramesh, E. Ma, L.J. Kecskes, L. Magness, R. Dowding, V.U.  
529 Kazykhanov, and R.Z. Valiev: *Acta Materialia*, 2006, vol. 54, pp. 77–87.

530 25 Y. Yu, H. Hu, W. Zhang, and X. Xu: *Journal of Alloys and Compounds*, 2016, vol. 685,  
531 pp. 971–7.

532 26 Z.-H. Zhang, F.-C. Wang, S.-K. Li, and L. Wang: *Materials Science and Engineering:*  
533 *A*, 2006, vol. 435, pp. 632–7.

534 27 Y. Yu, C. Ren, and W. Zhang: *International Journal of Refractory Metals and Hard*  
535 *Materials*, 2018, vol. 76, pp. 149–57.

536 28 S. Suwas and R.K. Ray: *Crystallographic Texture of Materials*, Springer, 2014.

537 29 S. Li and I.J. Beyerlein: *Modelling and Simulation in Materials Science and*  
538 *Engineering*, 2005, vol. 13, p. 509.

539 30 C. Deng, S.F. Liu, J.L. Ji, X.B. Hao, Z.Q. Zhang, and Q. Liu: *Journal of Materials*  
540 *Processing Technology*, 2014, vol. 214, pp. 462–9.

541 31 E. ASTM: *West Conshohocken, PA: ASTM International*, 2000, pp. 98–105.

542 32 F. Bachmann, R. Hielscher, and H. Schaeben: in *Solid State Phenomena*, vol. 160,  
543 2010, pp. 63–8.

544 33 C.N. Tomé and R.A. Lebensohn: *Los Alamos National Laboratory (USA) and*  
545 *Universidad Nacional de Rosario (Argentina)*.

546 34 C.N. Tomé: *Modelling and Simulation in Materials Science and Engineering*, 1999,  
547 vol. 7, p. 723.

548 35 J.W. Hutchinson: *Proceedings of the Royal Society of London. A. Mathematical and*  
549 *Physical Sciences*, 1976, vol. 348, pp. 101–27.

550 36 R.A. Lebensohn and G.R. Canova: *Acta Materialia*, 1997, vol. 45, pp. 3687–94.

551 37 H. Li, F. Larsson, M.H. Colliander, and M. Ekh: *Materials Science and Engineering: A*,  
552 2021, vol. 799, p. 140325.

553 38 R.A. Lebensohn, P.A. Turner, and G.R. Canova: *Computational materials science*,  
554 1997, vol. 9, pp. 229–36.

555 39 R.A. Lebensohn and C.N. Tomé: *Acta metallurgica et materialia*, 1993, vol. 41, pp.  
556 2611–24.

557 40 N.P. Gurao and S. Suwas: *Metallurgical and Materials Transactions A*, 2017, vol. 48,  
558 pp. 809–27.

559 41 C. Mondal, A.K. Singh, A.K. Mukhopadhyay, and K. Chattopadhyay: *Materials*  
560 *Science and Engineering: A*, 2013, vol. 577, pp. 87–100.

561 42 P. Gilormini, B. Bacroix, and J.J. Jonas: *Acta metallurgica*, 1988, vol. 36, pp. 231–56.

562 43 R. Becker: *Acta metallurgica et materialia*, 1991, vol. 39, pp. 1211–30.

563 44 C.N. Tomé, C.T. Necker, and R.A. Lebensohn: *Metallurgical and Materials*  
564 *Transactions A*, 2002, vol. 33, pp. 2635–48.

565 45 J.M. Rosenberg and H.R. Piehler: *Metallurgical Transactions*, 1971, vol. 2, pp. 257–9.

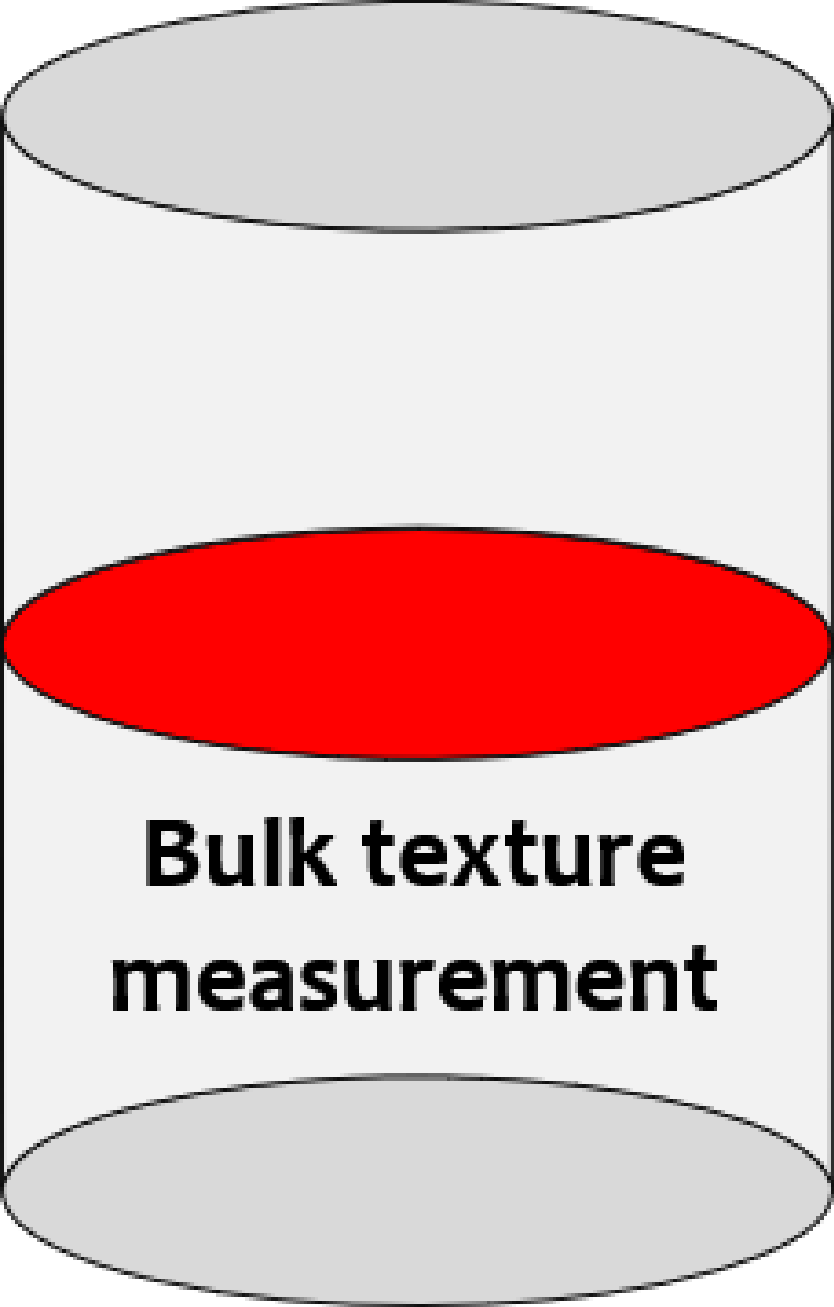
566 46 I.L. Dillamore, H. Katoh, and K. Haslam: in *Texture*, vol. 1, 1970.

567 47 T.B. Britton and J.L.R. Hickey: in *IOP Conference Series: Materials Science and*  
568 *Engineering*, vol. 304, 2018, p. 12003.

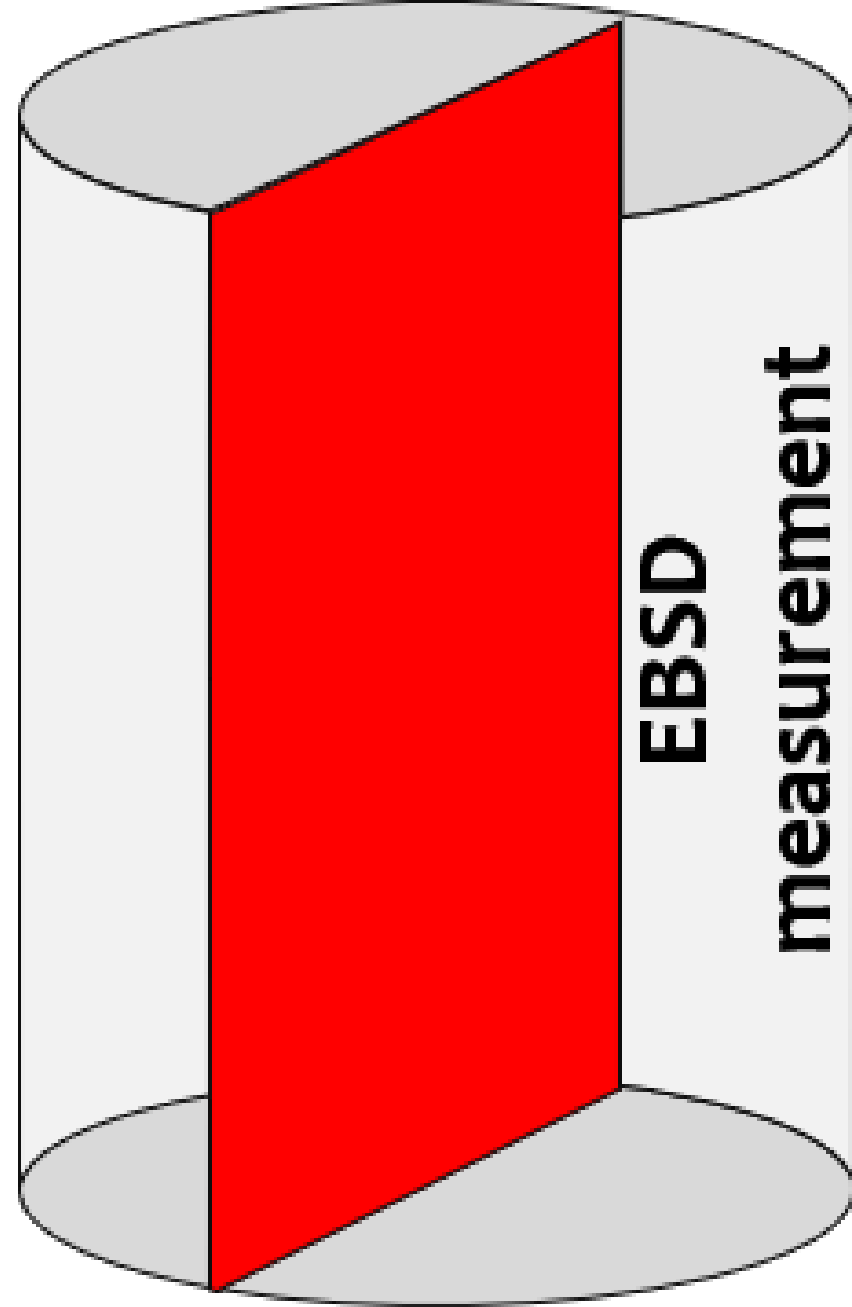
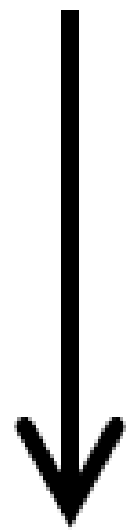
569 48 A.M. Korsunsky, K.E. Wells, and P.J. Withers: *Scripta Materialia*, 1998, vol. 39, pp.  
570 1705–12.

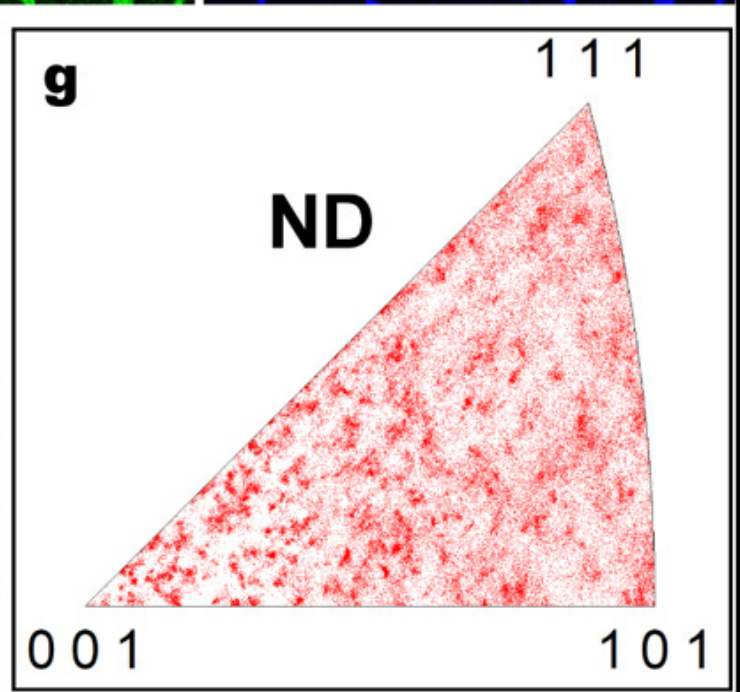
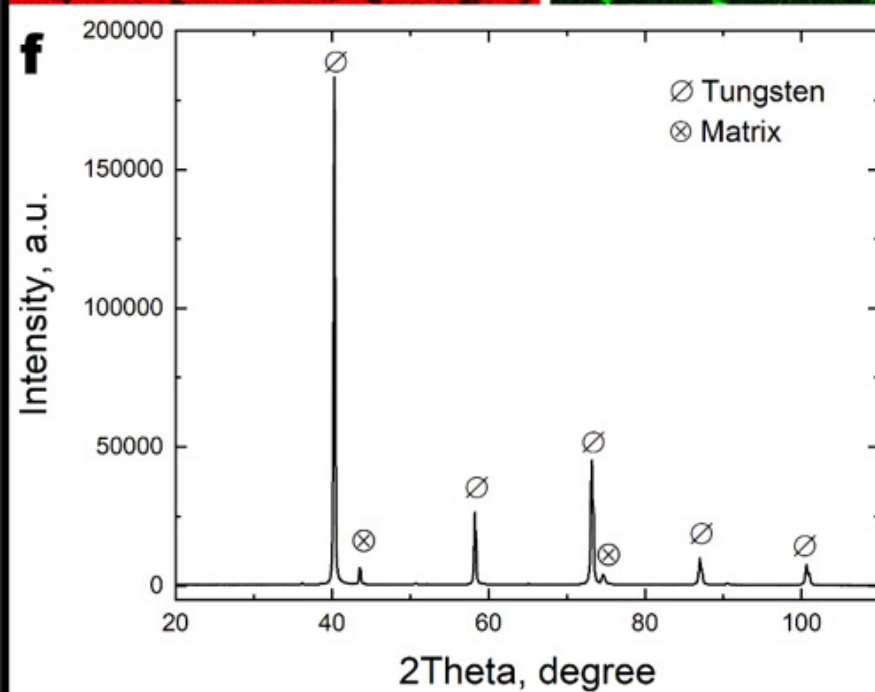
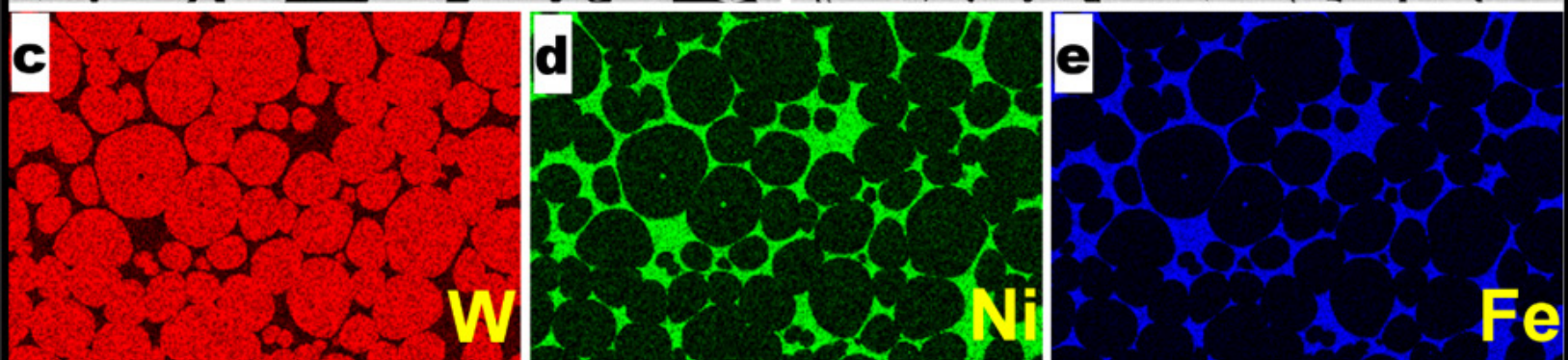
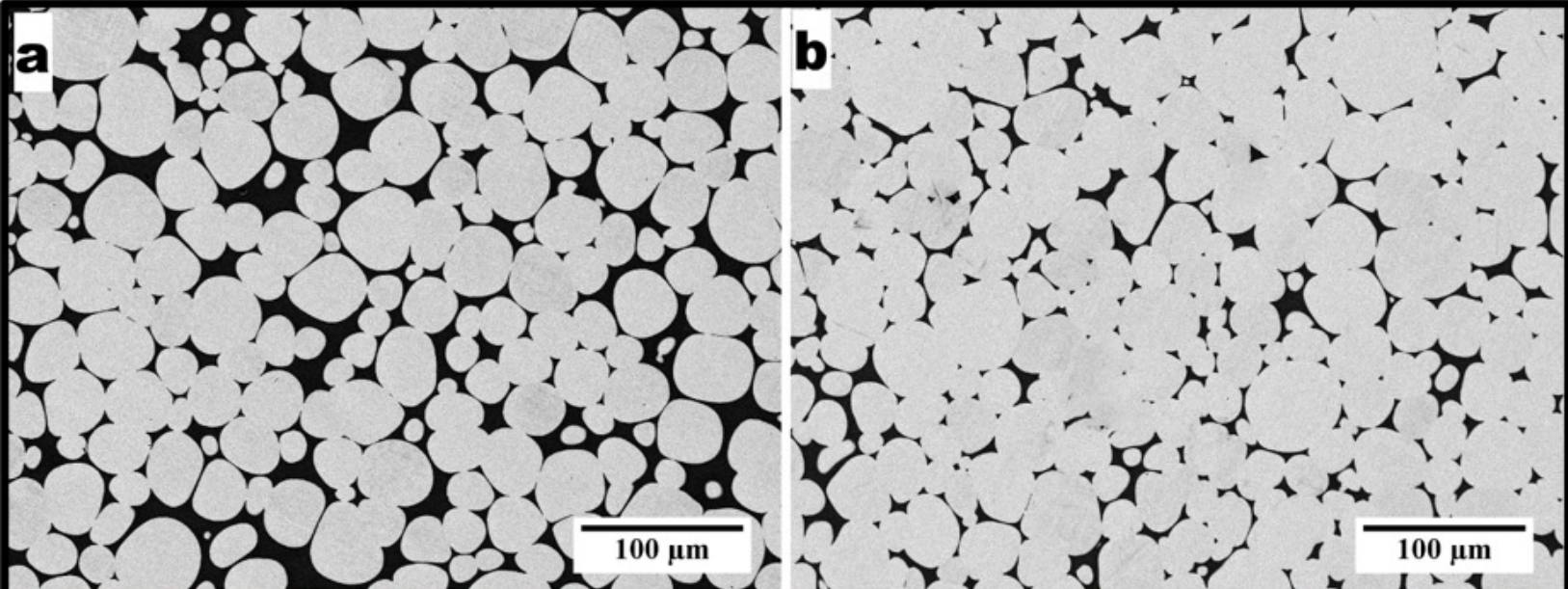
571 49 E.A. Calnan and C.J.B. Clews: *The London, Edinburgh, and Dublin Philosophical*  
572 *Magazine and Journal of Science*, 1951, vol. 42, pp. 616–35.

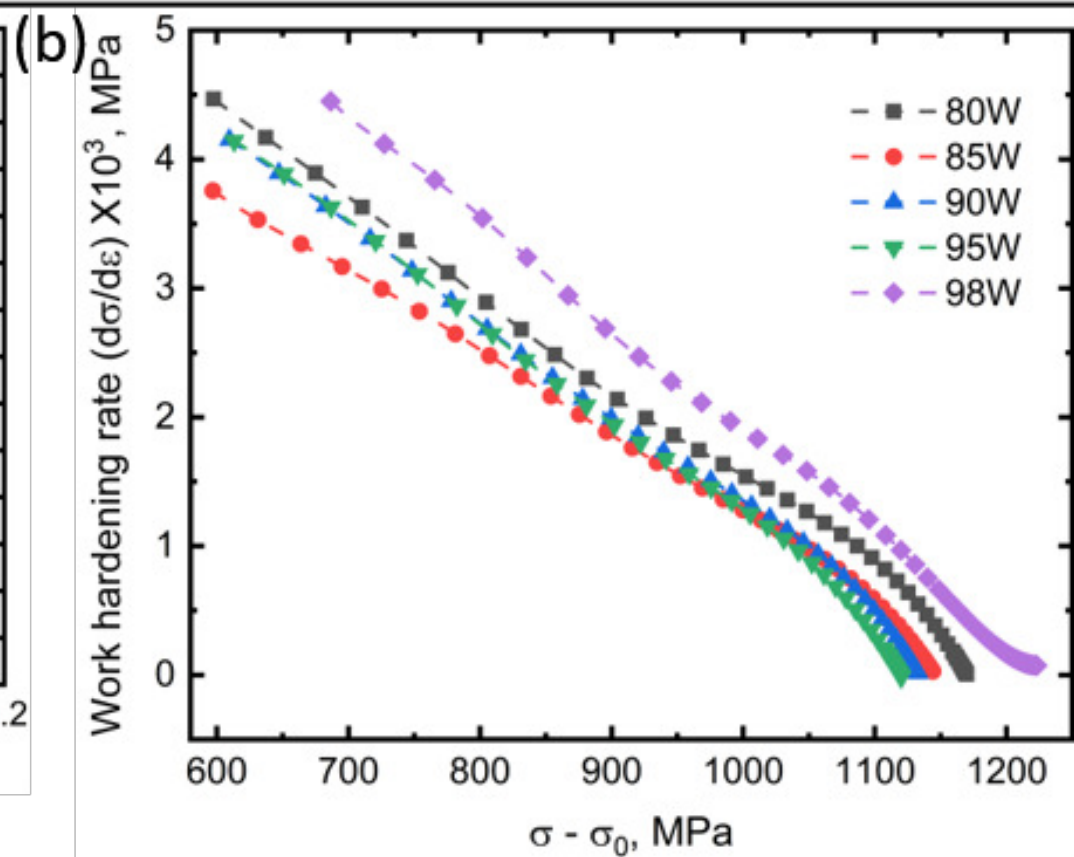
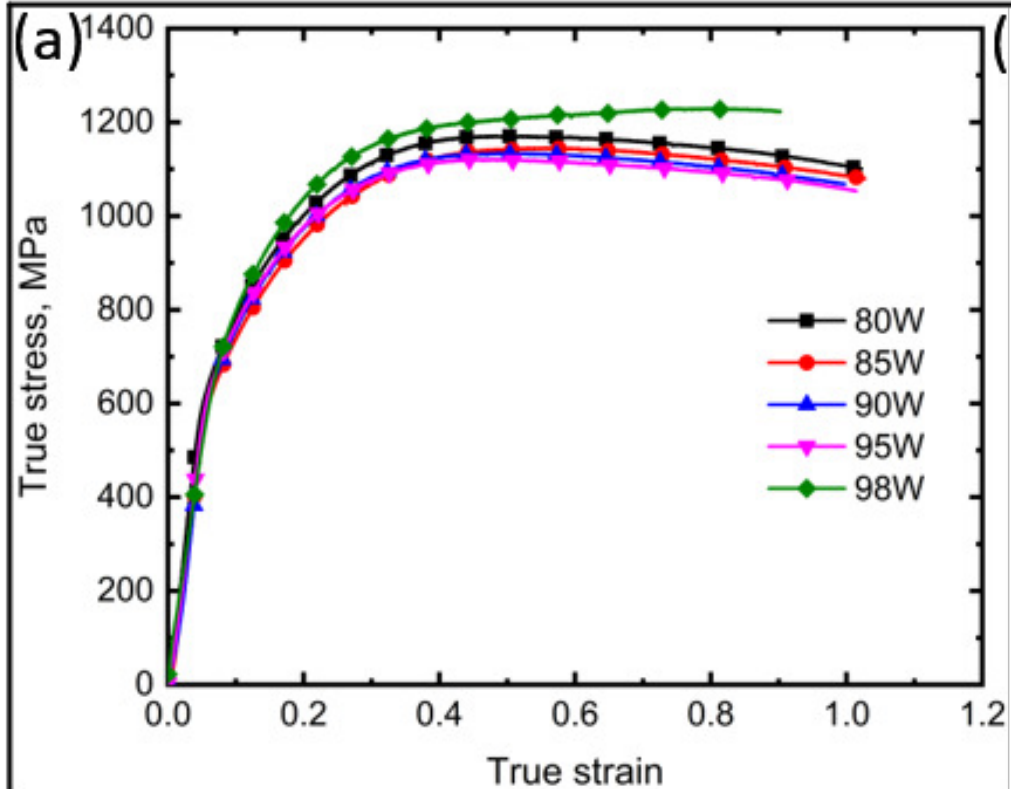
573



**Compression Direction**

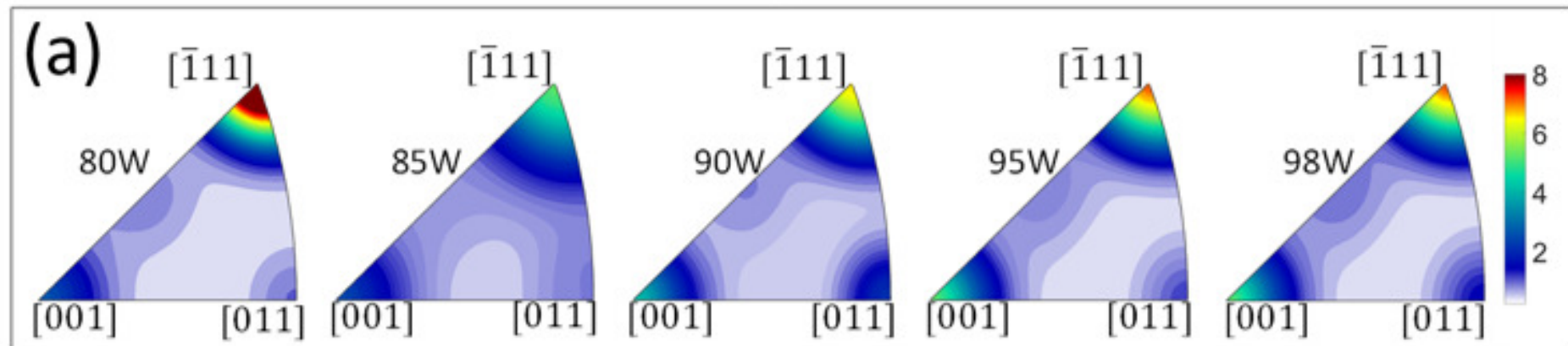




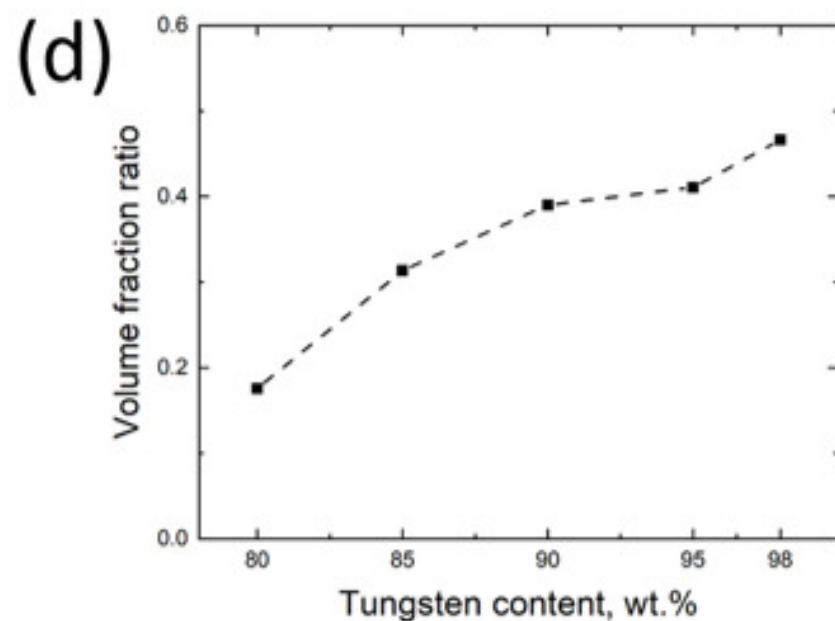
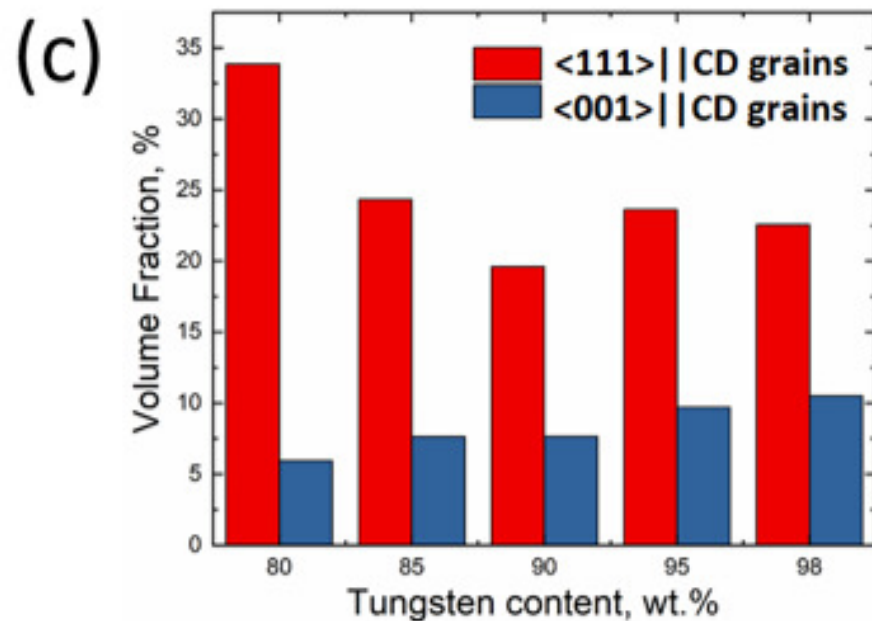
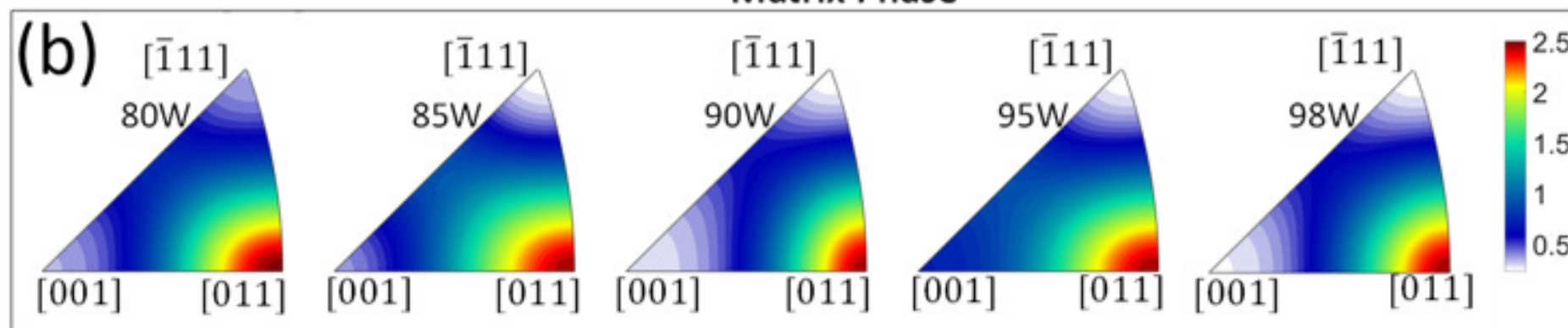




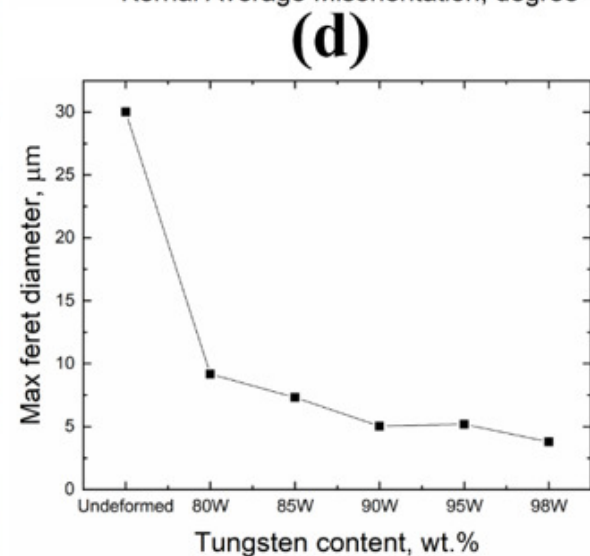
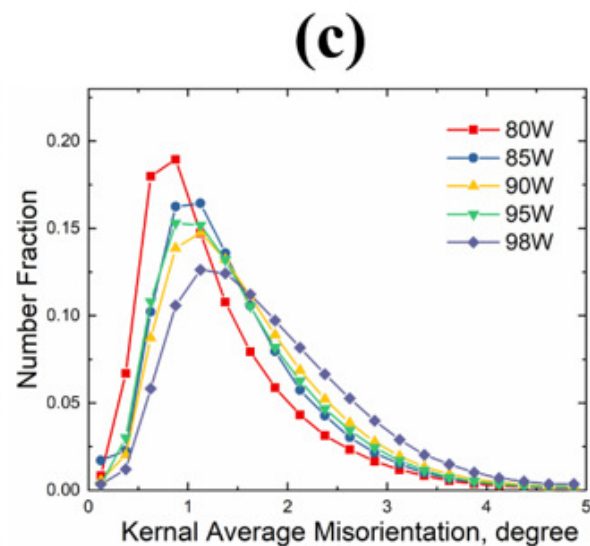
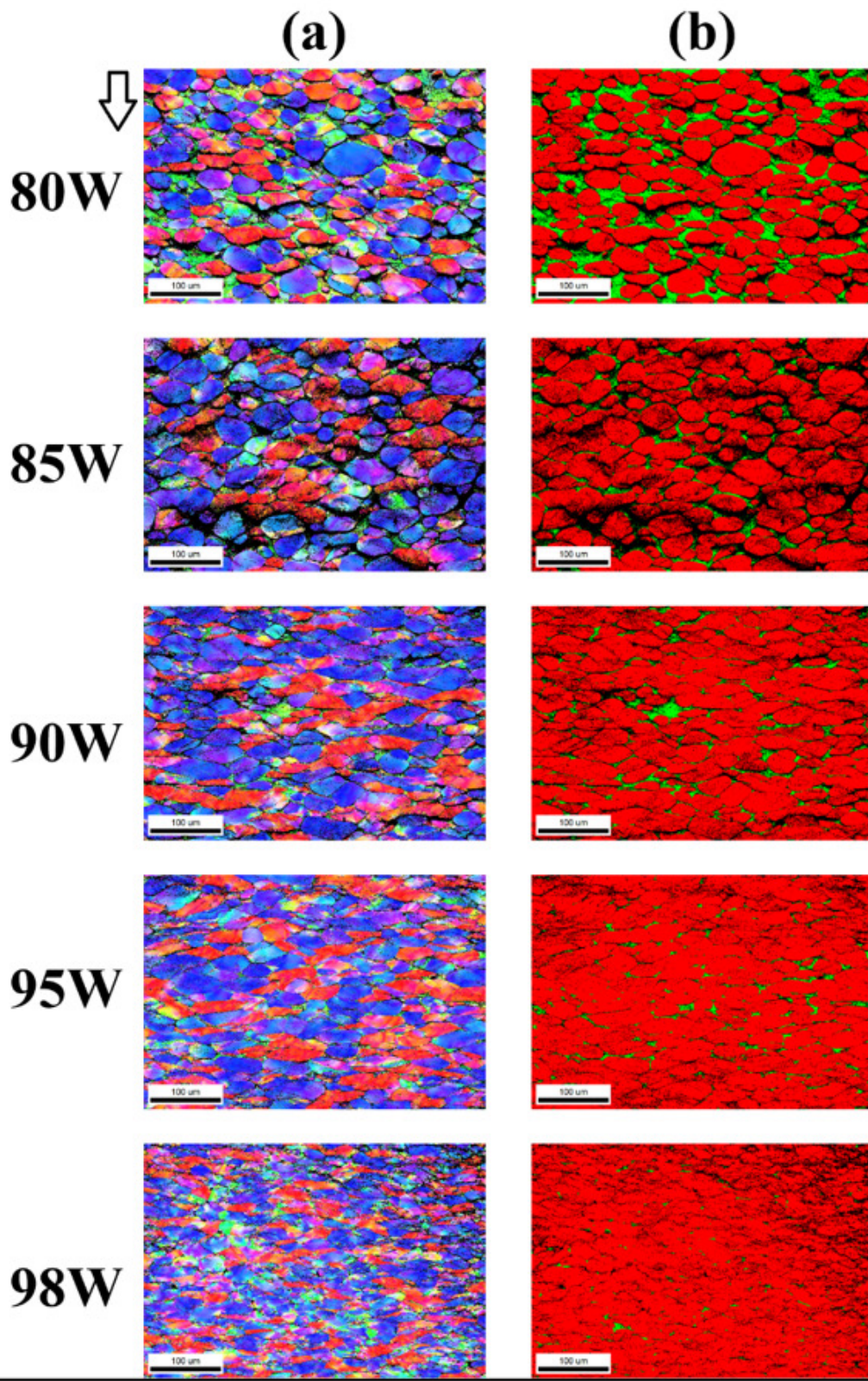
## Tungsten Phase



## Matrix Phase

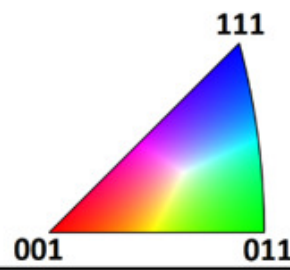






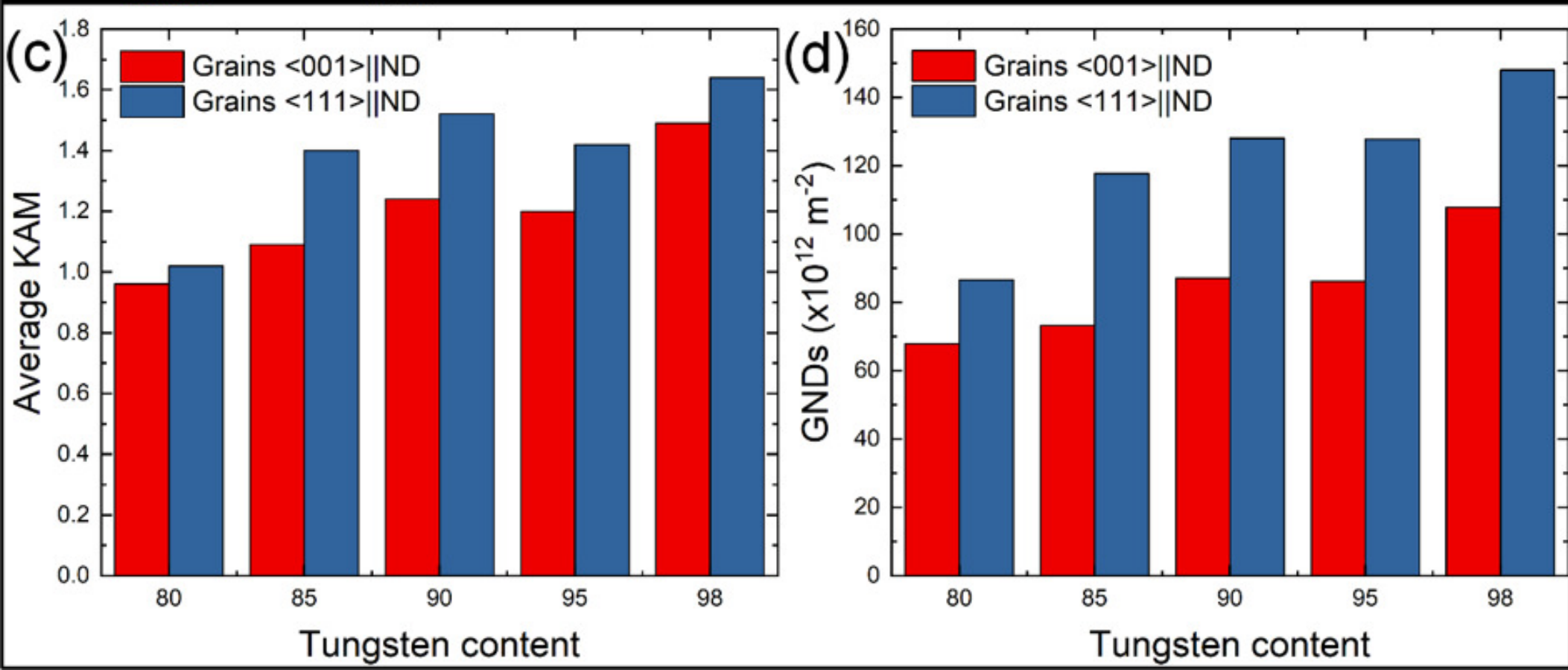
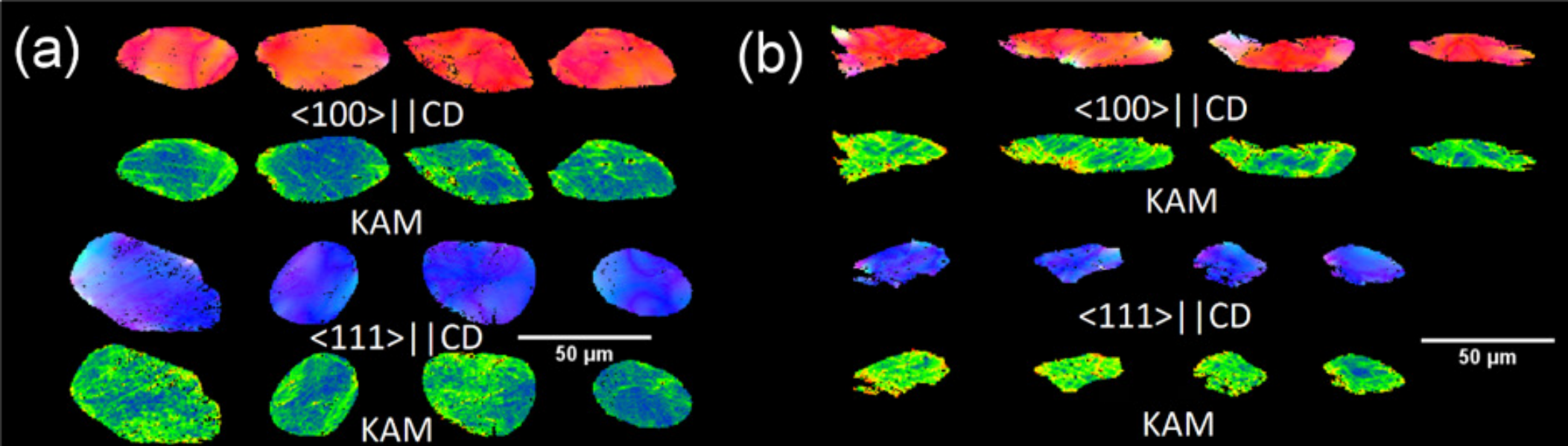
**(e)**  
Legends

IPF Maps



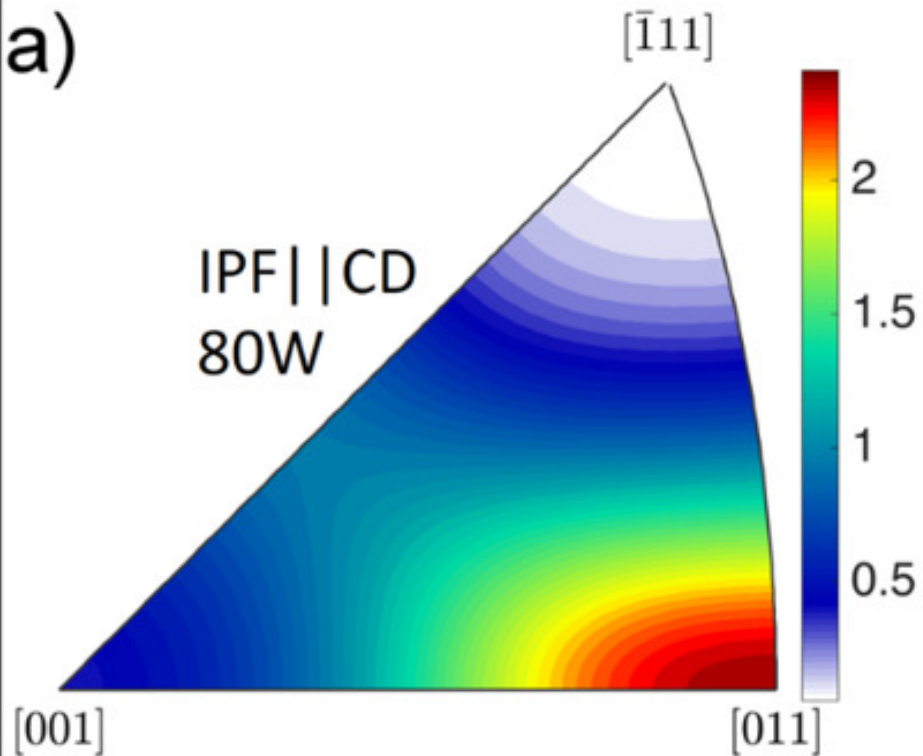
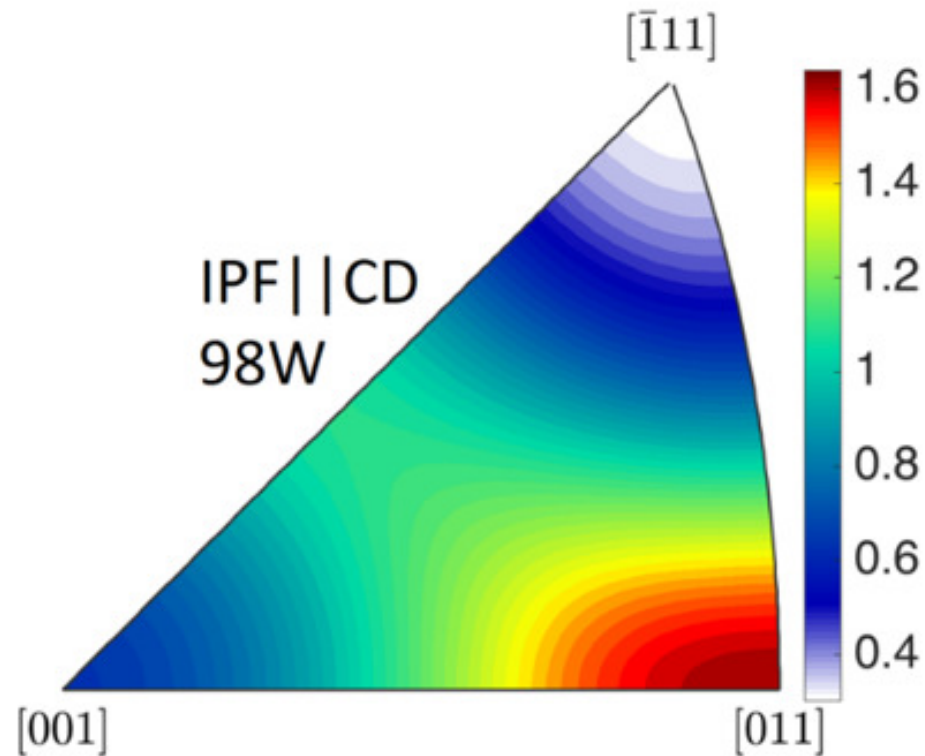
Phase  
Maps



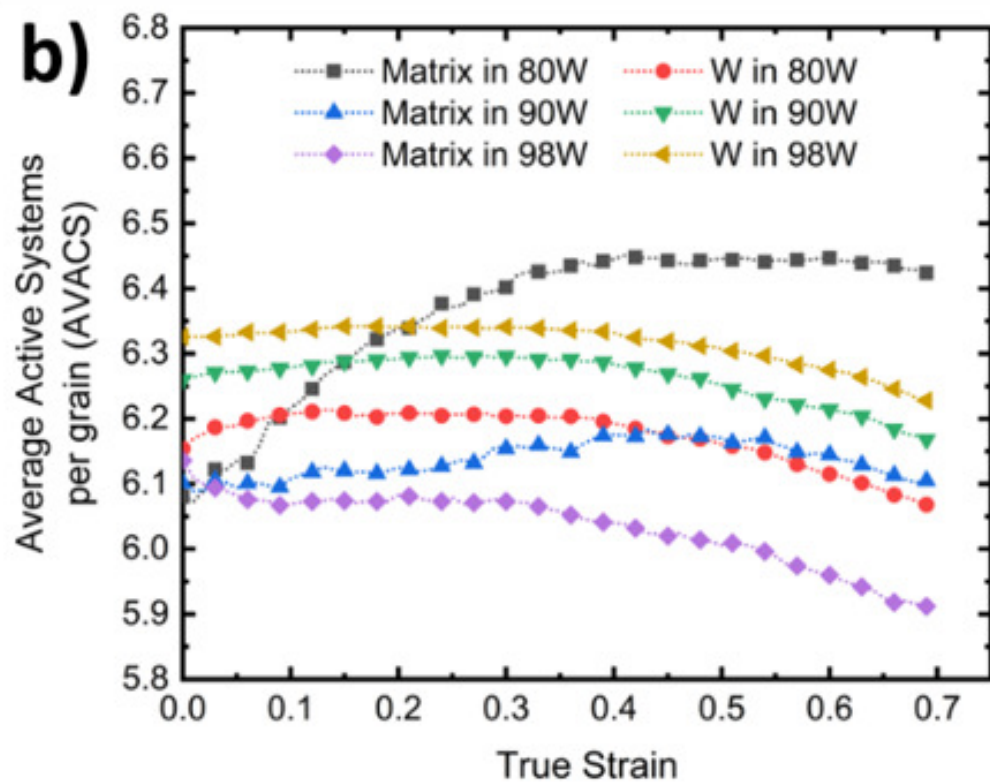




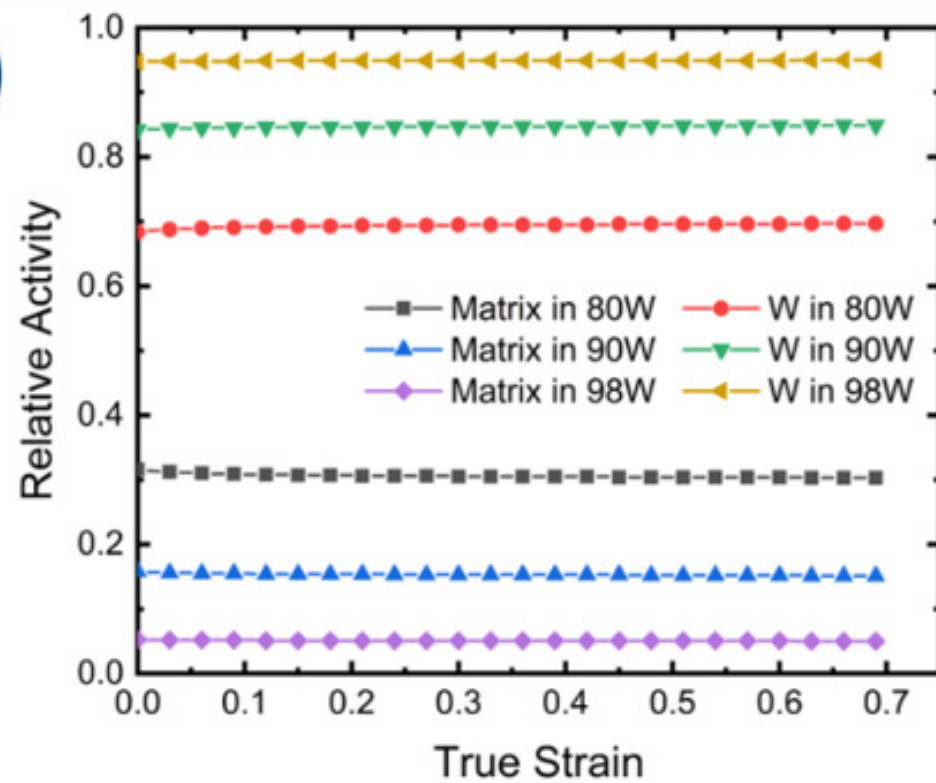
a)

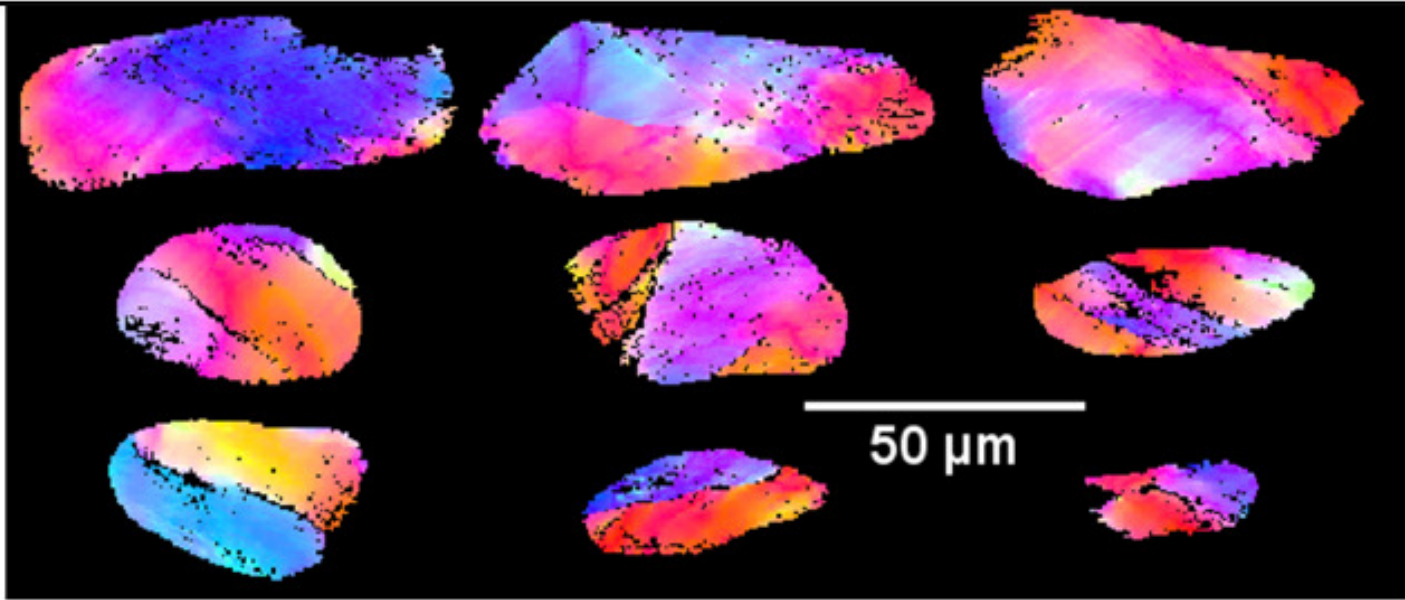
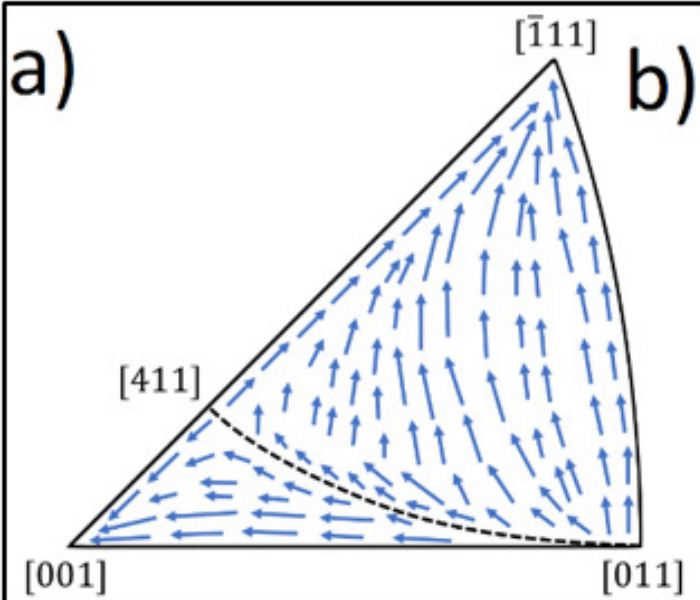
IPF || CD  
80WIPF || CD  
98W

b)



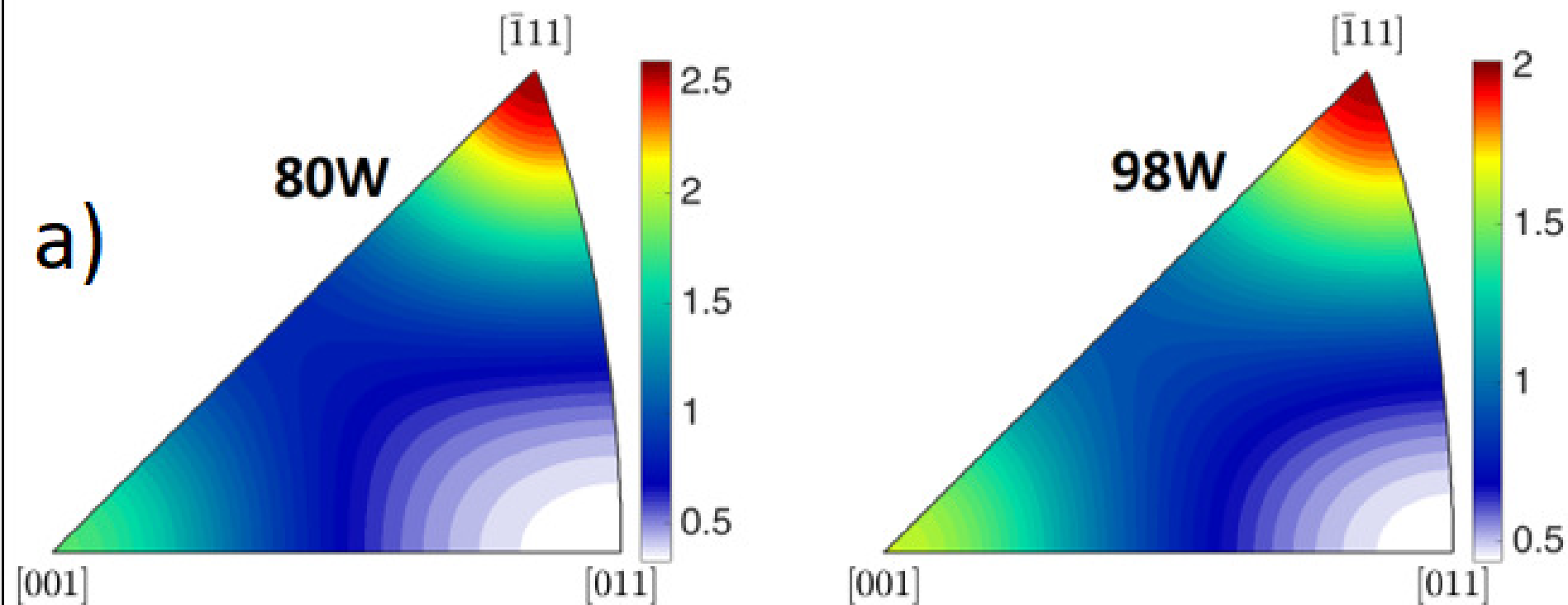
c)





# SECANT MODEL

a)



b)

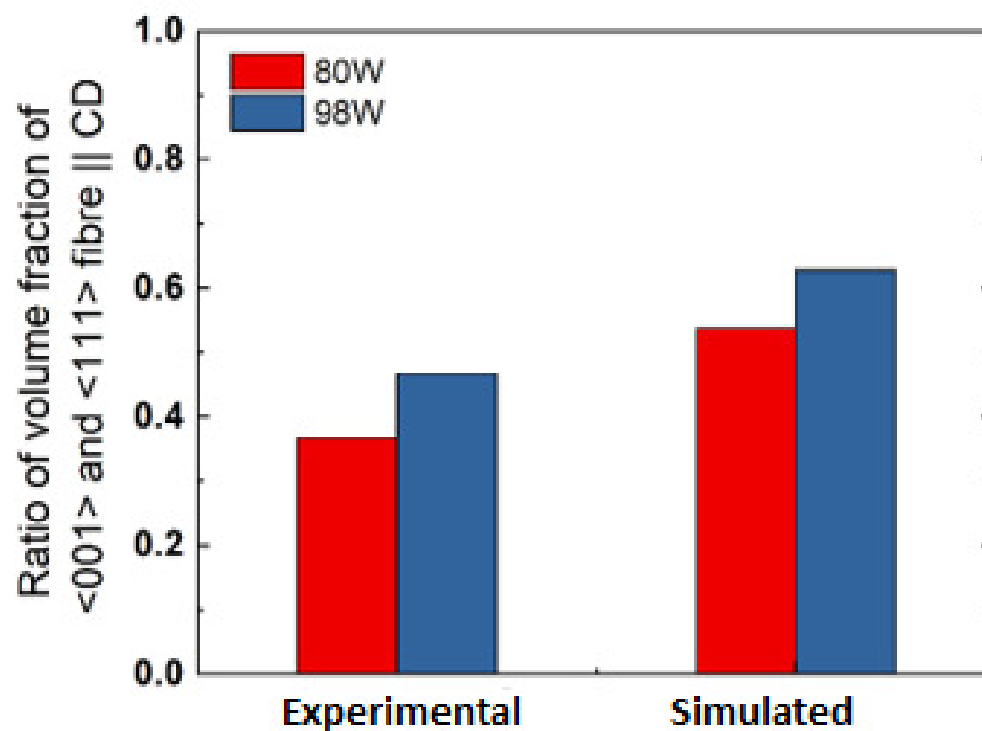


**Table 1** Composition of tungsten heavy alloy.

<b>Alloy</b>	<b>W (wt.%)</b>	<b>Ni (wt.%)</b>	<b>Fe (wt.%)</b>
80W-20M	80	14	6
85W-15M	85	10.5	4.5
90W-10M	90	7	3
95W-5M	95	3.5	1.5
98W-2M	98	1.4	0.6

**Table 2** Parameters for extended Voce hardening law

<b>Phase</b>	<b>Slip system family</b>	$\tau_0$	$\tau_1$	$\theta_0$	$\theta_1$
W	$\{\bar{1}10\} < 111 >$	$\tau_0$	235	355	0
	$\{11\bar{2}\} < 111 >$	$1.3 \tau_0$	350	100	20
	$\{12\bar{3}\} < 111 >$	$1.5 \tau_0$	200	100	10
Matrix	$\{111\} < \bar{1}10 >$	$0.6 \tau_0$	200	100	0

**Table 3:** Grain size and phase fraction of sintered WHA

<b>Sample</b>	<b>Grain Size of W (<math>\mu m</math>)</b>	<b>Phase Fraction of Matrix</b>
80W-20M	$21 \pm 10$	0.3
85W-15M	$20.7 \pm 10.4$	0.23
90W-10M	$22 \pm 13$	0.19
95W-5M	$20.2 \pm 10.3$	0.13
98W-2M	$20 \pm 12$	0.08